



HHS Public Access

Author manuscript

Bioorg Med Chem. Author manuscript; available in PMC 2022 March 15.

Published in final edited form as:

Bioorg Med Chem. 2021 March 15; 34: 115990. doi:10.1016/j.bmc.2020.115990.

Chemical Validation of a Druggable Site on Hsp27/HSPB1 using *In Silico* Solvent Mapping and Biophysical Methods

Leah N. Makley^{1,2,⊥}, Oleta T. Johnson^{1,⊥}, Phani Ghanakota², Jennifer N. Rauch¹, Delaney Osborn¹, Taia Wu¹, Tomasz Cierpicki³, Heather A. Carlson², Jason E. Gestwicki^{1,*}

¹Department of Pharmaceutical Chemistry and the Institute for Neurodegenerative Disease, University of California at San Francisco, San Francisco, CA 94158

²Department of Medicinal Chemistry, University of Michigan, Ann Arbor MI 48109

³Department of Pathology, University of Michigan, Ann Arbor MI 48109

Abstract

Destabilizing mutations in small heat shock proteins (sHsps) are linked to multiple diseases; however, sHsps are conformationally dynamic, lack enzymatic function and have no endogenous chemical ligands. These factors render sHsps as classically “undruggable” targets and make it particularly challenging to identify molecules that might bind and stabilize them. To explore potential solutions, we designed a multi-pronged screening workflow involving a combination of computational and biophysical ligand-discovery platforms. Using the core domain of the sHsp family member Hsp27/HSPB1 (Hsp27c) as a target, we applied mixed solvent molecular dynamics (MixMD) to predict three possible binding sites, which we confirmed using NMR-based solvent mapping. Using this knowledge, we then used NMR spectroscopy to carry out a fragment-based drug discovery (FBDD) screen, ultimately identifying two fragments that bind to one of these sites. A medicinal chemistry effort improved the affinity of one fragment by ~50-fold (16 μ M), while maintaining good ligand efficiency (~0.32 kcal/mol/non-hydrogen atom). Finally, we found that binding to this site partially restored the stability of disease-associated Hsp27 variants, in a redox-dependent manner. Together, these experiments suggest a new and unexpected binding site on Hsp27, which might be exploited to build chemical probes.

Graphical Abstract

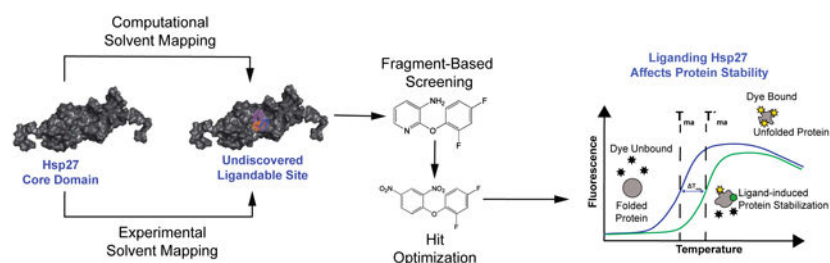
*Correspondence: Jason E. Gestwicki, Ph.D., Sandler Center, Room 311, University of California at San Francisco, San Francisco, CA 94158, (415) 502 7121, Jason.gestwicki@ucsf.edu.

⊥These authors contributed equally to the work.

Publisher's Disclaimer: This is a PDF file of an unedited manuscript that has been accepted for publication. As a service to our customers we are providing this early version of the manuscript. The manuscript will undergo copyediting, typesetting, and review of the resulting proof before it is published in its final form. Please note that during the production process errors may be discovered which could affect the content, and all legal disclaimers that apply to the journal pertain.

Declaration of interests

J. E. Gestwicki and L. N. Makley are co-founders of Viewpoint Therapeutics.



Keywords

small heat shock protein; undruggable; chaperone; neuropathy; DSF; thermal stability; solvent mapping

1. Introduction

Small heat shock proteins (sHsps) are a recondite class of ATP-independent molecular chaperones^{1,2} that aid in suppressing protein aggregation under stress conditions³. It is thought that these chaperones bind to unfolded proteins, keeping them soluble until they can be refolded. Structurally, these chaperones are defined by a conserved α -crystallin core domain (ACD), flanked by disordered N- and C-terminal extensions⁴. Each of these motifs are involved in extensive protein-protein interactions (PPIs). Specifically, the ACD is composed of six β -strands that form an immunoglobulin fold and two of these β -strands, associated in an antiparallel fashion, form a stable dimer interface. Additional contacts involving the N- and C-terminal extensions mediate high-order assembly of these dimers into larger oligomers^{5–8}. In theory, this architecture creates potential opportunities for drug discovery, such as targeting the intra- or inter-molecular PPI surfaces. However, the sHSP oligomers are polydisperse (typically composed of 10–20 dimers) and dynamic in response to cellular stress^{5,9}. Thus, it is not clear which of the transient pockets might allow chemical ligands to bind with good affinity.

To explore these questions, we focused on heat shock protein 27 (Hsp27/HSBP1). This member of the sHSP family is of interest because mutations in Hsp27's ACD, including R127W and S135F, are closely linked to diseases, such as distal hereditary motor neuropathy and Charcot-Marie-Tooth disease^{10,11}. These mutations are known to destabilize Hsp27 oligomers and aberrantly increase its chaperone activity¹². This observation is consistent with an emerging model in which smaller, less stable Hsp27 oligomers are more active^{5,9}, at least in some contexts. This idea is further supported by the fact that an intermolecular disulfide bond formed at Hsp27's dimer interface is known to limit its conformational flexibility and, consistent with the model, decrease chaperone activity^{13–15}. Together, these observations suggest that one therapeutic objective, at least in a subset of Hsp27-related diseases, may be to identify drug-like molecules that bind and partially restore the stability of disease-associated mutations, such as R127W and S135F. However, there are no known binding pocket(s) for small molecules on Hsp27.

A number of techniques have been developed to identify binding sites on other “undruggable” targets, including computational methods for suggesting sites¹⁶ and

fragment-based screening approaches¹⁷. Here, we combine computational and experimental platforms towards the discovery of proof-of-principle ligands for Hsp27. Using this combination of approaches, we identified a promising and previously unexplored binding site within Hsp27's ACD and found that a chemical fragment ($K_d > 1$ mM) could be matured through a medicinal chemistry campaign to bind with good affinity ($K_d \sim 16$ μ M) and ligand efficiency (0.32 kcal/mol/non-hydrogen atom). Importantly, the resulting probe partially stabilized a disease-associated Hsp27 mutant *in vitro*, suggesting that this site might be tractable for further development. While additional work is required to increase affinity, these studies provide a starting point for Hsp27 drug discovery and, potentially, for exploration of other sHSPs.

2. Results and Discussion

2.1 Identification of three binding sites on Hsp27c.

A key challenge with Hsp27 is that binding sites for ligands are not known. To explore this question, we focused on the dimeric, Hsp27 core domain (Hsp27c; residues 79–176), because high-resolution structures are available^{6,8} and this region includes the disease-associated mutations, R127W and S135F. In this manuscript, we will use the numbering system of the Hsp27c domain to discuss these hereditary mutations, such that R127W in full length Hsp27 is referred to as R49W and S135F is S57F. In the Hsp27c structure, the S57F mutation is located on the dimer interface, while the R49W mutation is in a flexible region ~ 5 Å away (Figure 1A, 1B). We were also interested in this region because Hsp27c's dimer interface includes a single cysteine (Figure 1C), and in the NMR structure, the cysteine from one protomer is located directly across from the cysteine of the other protomer. This cysteine gives Hsp27c redox sensing properties, through reversible formation of disulfide bonds^{6,11,18}. Thus, in addition to being structurally tractable for ligand discovery, Hsp27c is also a hotspot for disease-associated mutations and redox signaling.

To identify putative binding sites on Hsp27c, we employed mixed-solvent molecular dynamics (MixMD). In a MixMD experiment, the structure is placed in a virtual box of mixed aqueous and organic solvent molecules^{19,20}. During a molecular dynamics (MD) simulation, these organic probes tend to cluster at putative ligand-binding pockets on the surface of the protein as they outcompete water²¹. In the case of Hsp27c, we chose three organic solvent probes selected to represent drug-like interactions: acetonitrile (hydrophobic), pyrimidine (aromatic), and isopropanol (hydrogen-bond donating and accepting). The high-resolution structure of Hsp27c (PDB 2N3J) in the oxidized state was then used in a 20 ns MD simulation incorporating full protein flexibility. From this analysis, three distinct binding sites were highly occupied by each of the three solvent probes (Figure 2A). One of the sites, labeled Site 1, corresponds to a symmetry-related groove at the “top” of the dimer interface. The second site (Site 2) was observed along the outer edge of the β -sandwich, in a pocket formed by the $\beta 4$ and $\beta 8$ strands. The third site (Site 3) occupied a concave pocket on the opposite side (“bottom”) of the dimer interface from Site 1.

Computational methods for identifying binding sites are becoming used with greater frequency^{16,21,22,24,25}. However, few studies have attempted to correlate these findings with experiments. Experimental solvent mapping has been used to support computational

predictions for drug-like fragments²³; however, a prospective, side-by-side comparison using the same probe solvents has not, to our knowledge, been previously reported. Towards that goal, we utilized HSQC NMR spectroscopy to perform the experimental equivalent of the MixMD study, titrating pyrimidine, isopropanol, or acetonitrile into a buffered solution of uniformly ¹⁵N-labeled Hsp27c. The final concentrations of the solvents ranged from 5 to 30 mM. From the resulting spectra, backbone chemical shift perturbations (CSPs) exceeding two standard deviations (SD) were interpreted as a proximal solvent interaction. In these titrations, we found that each of the three solvents produced significant and defined CSPs. Strikingly, these CSPs clustered around the same three regions, Site 1, Site 2 and Site 3 (Figure 2B), that were predicted from the MixMD simulations. Thus, both the computational and experimental studies aligned to suggest that there are at least three binding sites on Hsp27c.

Before exploring the ‘druggability’ of these sites further, we explored whether any of them might be supported by literature reports. In crystal structures of a related ACD, we noticed that the crystallization additives methylpentanediol and sulfate populate Site 1, suggesting that this pocket sometimes binds small molecules in other sHSPs²⁶. Site 2 is located in a hydrophobic groove formed by the β 4 and β 8 strands of the core domain, which is known to be a hot-spot for intra- and inter-molecular protein-protein interactions (PPIs). For example, this region binds to an IXI palindromic motif, which is located in the C-terminal extension of Hsp27^{5,27,28}, to stabilize oligomers²⁷. In addition, the co-chaperone BAG3 also binds to Site 2, using its own IXI motifs²⁹. In contrast, we were unable to find any literature precedent for Site 3 ; therefore, we focused our efforts on the validation of this newly identified site on Hsp27c.

2.2 Validation of Site 3 through fragment-based drug discovery.

To explore Site 3, we applied protein-observed, fragment-based drug design (FBDD) by NMR. In this approach, low molecular weight fragments are expected to bind weakly, but with high ligand efficiency, causing measurable perturbations in the chemical shift values for amino acid residues at or near the binding site¹⁷. One advantage of FBDD by NMR is that the fragment-binding sites are identified as part of the routine screening process; here allowing us to specifically search for those that perturb residues in Site 3. In the initial experiments, uniformly ¹⁵N-labeled Hsp27c was used in a protein-observed HSQC screen of the Maybridge RO3 library of ~1,000 fragment molecules. To increase throughput, we multiplexed the fragments in groups of 20, using 125 μ M Hsp27c and 250 μ M of each fragment (Figure 3A). We found that thirty-three mixtures exhibited large (>8 Hz) CSPs. Hit rates from NMR-based FBDD screens are sometimes used as a metric for the potential ‘druggability’ of a protein target. For example, in Hajduk’s influential analysis, targets producing experimental NMR hit rates higher than 0.2% are associated with subsequent medicinal chemistry campaigns that tend to result in optimized hits with tight affinity (<300 nM)³⁰. Here, for a library of 1,000 fragments, that value would be expected to be ~2 hits, so we were encouraged by the relatively high number of active mixtures in the Hsp27c screen. To identify the active fragment(s) within these mixtures, the six pools with the strongest CSPs were then deconvoluted by testing the ~110 isolated fragments. This process identified

4 potential hit molecules (0.4%), again suggesting that Site 3 of Hsp27c might be more druggable than previously envisioned.

Next, we re-synthesized the four hit molecules using known synthetic routes (Figure 3B). Synthesis of compound **1** proceeded from Suzuki coupling (scheme 1), while compound **2** was afforded by thionation of a commercial starting material, followed by ring closing of the thiazole (scheme 2). The third molecule was synthesized by base-catalyzed C-S coupling, yielded compound **3** as a mixture of stereoisomers which was isolated as 78% E-olefin (scheme 3a; compound **3a**). Finally, the remaining hit fragment, compound **4**, was synthesized through a Williamson ether coupling, followed by reduction to the aniline (scheme 4). These molecules were characterized for identity and purity and then tested in the NMR assay. In these experiments, neither compound **1** nor **2** bound to Hsp27c (data not shown), suggesting that they are either false positives or have very weak affinity. Likewise, the E-olefin compound **3a** did not bind to Hsp27c by NMR, prompting us to explore whether the stereochemistry around the olefin might be misannotated in the library. Upon inspecting the ¹H spectra from original screening sample, we noted that the ³J_{HH} coupling constant for the alkenyl protons was characteristic of the Z-olefin (Figure S1), prompting us to synthesize the Z-olefin (compound **3b**) via an alternate synthetic route (100% ee; scheme 3b). Indeed, the Z-olefin weakly bound Hsp27c (data not shown). Finally, we found that compound **4** bound Hsp27c in STD-NMR experiments (Figure S2) and produced strong CSPs in both Site 1 and Site 3 by HSQC NMR studies (data not shown). Based on these results, we focused on creating analogs of compound **4**.

2.3 Exploring the structure-activity relationships of ligands to Site 3.

To probe whether Site 3 could bind tightly to ligands, we created a library of 48 analogues of compound **4**. Briefly, analogs were synthesized using the known route (see Figure 3B; scheme 4), varying the substitutions on the rings adjacent the bridging ether. In addition, we supplemented this synthetic effort with the purchase of commercial analogs (denoted with an asterisk, Table 1; Table S2). In the initial tests, each molecule was dissolved in DMSO and screened at a single concentration (250 μM) in the HSQC NMR binding assay. If significant (>8 Hz) CSPs were observed relative to the vehicle control, then a full titration series was performed. When possible, a plot of CSPs versus concentration was fit with a hyperbolic one-site binding model to extract an apparent affinity (K_d) (Table 1; Figure S3).

Binding of compound **4** was not saturable during titration (up to 1 mM), suggesting weak binding. However, we found that the unreduced nitropyridine at the 3-position, compound **5**, bound more tightly, giving saturable curves in the HSQC titration and an apparent affinity of ~177 μM (Table 1). Moving the nitro substitution to the 5-position (compound **6**) resulted in a further improvement in affinity (~63 μM). In the context of the 5-nitro substitution, replacement of the pyridine ring with a benzyl had little effect (~69 μM; compound **8**), suggesting that the heteroatom is not required. Likewise, removing a fluoro-group (compound **7**) did not significantly alter affinity (~65 μM). However, removing both the pyridine nitrogen and the fluoro group (compound **9**) resulted in a modest boost in affinity (~23 μM). Appending nitro groups at both the 3- and 5- positions did not improve on this affinity (compound **10**; ~47 μM) and neither did moving the single fluoro group from the p-

to m-position (compound 11; ~80 μM). Finally, we tested the effects of adding both nitro and both fluoro groups (compound 12) and found that this analog had a promising K_d (~16 μM). This fragment represents a ~50-fold improvement in affinity from the original hit. Importantly for FBDD, the ligand efficiency^{31,32} (compound 12; LE = 0.32 kcal/mol/non-hydrogen atom) was not significantly decreased during this optimization.

The analogs tested thus far suggested that the position of the nitro and fluoro groups might be more important than their electronic properties. To further probe that idea, we synthesized compound 13, shifting one of the nitro groups, and found that it had significantly worse affinity (70 μM). Similarly, shuffling the fluorines on the right-hand ring resulted in compounds 25–27, which did not bind. Together, these results suggested that the position of the substituents is indeed important. To explore possible steric effects further, we designed and tested a series of additional analogs with larger substitutions. Interestingly, a nitrile could be accommodated in the 4-position (compound 17), but a trifluoromethyl group cannot (compound 37). Replacement of the fluorines with other halogens, a trifluoromethyl group, methyl groups, an aldehyde, or a carboxylic acid was poorly tolerated (compounds 24, 28–32). Thus, only small substitutions seemed to be accepted on this side of the molecule. Next, we explored the effects of the bridging ether; replacing it with a sulfur or nitrogen atom (compounds 43 and 44) removed activity, perhaps because the permissible orientations of the two planar rings relative to one another are affected. Similarly, insertion of a carbonyl, as in compounds 46 or 47, abolished binding. We hypothesized that introducing a third ring system might allow for expanding beyond the pocket, so created compounds 48–51; however, no CSPs were observed from these larger molecules. Together, the initial structure-activity relationships (SAR) suggest that this pocket in Site 3 might have restricted size. In summary, the best molecule from this campaign was compound 12 (1-(2,4-difluorophenoxy)-2,4-dinitrobenzene), which we used to further explore Site 3.

First, we needed to verify that compound 12 bound preferably to Site 3. In the HSQC titration series, addition of 12 induced CSPs on both the “top” and “bottom” of the ACD dimer (Figure 4B). Thus, to distinguish Site 1 from Site 3, we mutated residues in these pockets and tested binding of 12 to the mutants. First, we confirmed that the mutants were folded properly, as determined by HSQC spectra (Figure S4). Strikingly, we found that several mutations in Site 3 reduced (e.g. H46A) or completely abolished (e.g. R58A, F60A, and R62A) binding (Figure 5). Conversely, mutations in Site 1 (C59A, T61L, L21A) had only minor effects on the apparent binding affinity (2–4 fold). Residues V23A and I56A in Site 3 also seemed to play less important roles (affinity weakened by only ~4-fold). These studies suggest that compound 12 engages Site 3, likely via contacts with residues H46, R58, F60, and R62. To further support this idea, we also docked compound 12 to Hsp27c, with the best pose showing interactions between the molecule and the side chains of R58, F60 and R62 (Figure S5). Together, these findings indicate that Site 3 is a *bona fide* ligand-binding pocket, which could be suitable for further fragment expansion.

2.4 Ligand binding to Site 3 partially stabilizes Hsp27 mutants.

To evaluate the consequences of compound 12 binding, we measured its effects on the stability of full length Hsp27 by Differential Scanning Fluorimetry (DSF). In a typical DSF

assay, an environmentally sensitive dye, such as 1-anilinonaphthalene-8-sulfonic acid (1,8-ANS), is mixed with the protein and heated, such that the fluorescence *vs* temperature curve can be used to determine the protein's apparent melting temperature (T_{ma}) (Figure S6A). In the case of more complex proteins, such as those forming oligomers^{33,34}, it is common for multiple T_{ma} values to be observed (Figure S6B). In both cases, it is expected that ligand binding would increase the T_{ma} (T_{ma}) (Figure S6C), where the ligand could theoretically affect T_{ma1} , T_{ma2} or both. Given the known effects of both oxidation and mutation on Hsp27 stability, we recognized DSF as a potentially powerful tool to probe effects of compound **12** under combinations of different redox and mutational states.

As a first step, we compared the DSF curves from wild type (WT) Hsp27 and the corresponding S57F and R49W mutants (Figure S7). As expected, fitting the DSF data for Hsp27 using DSFWorld³⁵ resulted in at least two distinguishable melting transitions: T_{ma1} (~55 °C) and T_{ma2} (~67 °C). This result is consistent with observations from circular dichroism (CD) experiments, performed on either Hsp27 and its mouse homolog Hsp25^{36,37}, in which two melting transitions were also reported. Although it is difficult to ascribe specific structural states to these melting transitions, the low temperature transition (T_{ma1}) might correlate with perturbations of the oligomer structure, while the high temperature transition (T_{ma2}) is proposed to correlate with unfolding of the Hsp27 monomer. Regardless, we considered the two melting transitions (T_{ma1} and T_{ma2}) to be potentially diagnostic of Hsp27 structure and stability.

Using DSF, we explored the effects of the disease-associated mutations, S57F and R49W, on melting transitions. As mentioned above, S57F and R49W are known to decrease oligomer size^{12,14}; thus, we hypothesized that they might produce lower T_{ma1} and/or T_{ma2} values. Indeed, the S57F mutant showed a dramatic decrease (~8 °C) in both T_{ma} values relative to the WT protein (Table 2; Figure 6A). Interestingly, the R49W mutant only had one observable T_{ma} . It is known that R49W adopts a less stable, monomeric state^{12,14}; thus, it is possible that the two transitions overlap under these conditions. Regardless, the single observed T_{ma} for R49W was not significantly different from WT Hsp27 (Table 2; Figure 6A), suggesting that the DSF assay may only be sensitive enough to study a subset of disease-associated Hsp27 mutants.

Next, we explored whether compound **12** might partially stabilize the Hsp27 proteins, especially S57F. However, when we treated Hsp27c (WT) or the S57F and R49W mutants with compound **12** (10 μ M), there was minimal effect on the mutants (here, defined as < 2 °C) and a modest decrease in T_{ma1} and T_{ma2} for the WT (~3 to 4 °C; Figure 6B). While this result was initially surprising, we noted that these experiments were performed using the oxidized form of Hsp27c, in which the intra-protomer disulfide might be expected to stabilize the system. Thus, we decided to ask whether compound **12** might impact the mutants in the physiologically relevant, reduced state. In the presence of DTT, the S57F mutant was again dramatically unstable (~4 to 6 °C) compared to WT (Figure 6C). Interestingly, in the reduced state, the sample of R49W yielded two clear melting transitions (T_{ma1} and T_{ma2}), which were both unchanged from the WT. Finally, when we treated these samples with compound **12** (10 μ M), it stabilized S57F (~3 to 4 °C) and modestly stabilized R49W (0.6 to 2.4 °C), with little effect on WT (Figure 6D). Together, the results of these

DSF experiments show that compound **12** could partially restore the stability of S57F Hsp27c, suggesting that Site 3 might be a good choice for further development.

3. Summary and Conclusion

The identification of druggable sites is a challenge in complex, dynamic systems, such as Hsp27. Indeed, many promising drug targets, including protein complexes and proteins with high intrinsic disorder, share this issue³⁸. Both computational and experimental methods have been developed to identify potentially druggable sites in these types of examples. Here, we sought to combine these methods to identify and exploit putative sites on Hsp27c. Of the HSPs, Hsp27 is a particularly interesting drug target^{39–45} and multiple therapeutic modalities have been explored to inhibit this protein, including antisense oligonucleotides⁴², peptide aptamers^{46,47} and small molecules^{48,49}. However, druggable binding sites on Hsp27 had not been well defined, which limits efforts at structure-based design.

In this work, we identified three binding sites on the surface of Hsp27's ACD and discovered a scaffold that binds to the previously uncharacterized, Site 3. We also performed initial optimization of the lead fragment to produce a ligand, compound **12**, with good affinity (~16 μ M) and promising ligand efficiency (0.32 kcal/mol/non-hydrogen atom). The discovery of ligands that bind Site 3 is especially advantageous due to its location at the Hsp27 dimer interface. Cysteine disulfide formation and the disease-associated mutation S57F both occur at the dimer interface, each causing changes in the overall stability and, as a result, the chaperone activity of the protein. DSF experiments showed that compound **12** partially stabilizes the S57F Hsp27 mutant, dependent on its redox state, highlighting the potential utility of compound **12** as a pharmacological chaperone. Future work will be needed to develop the affinity and selectivity of these chemical ligands, which we speculate represent a valuable starting point for the optimization of useful Hsp27 probes.

4. Experimental Section

4.1 Mixed-Solvent Molecular Dynamics (MixMD).

MixMD simulations were conducted as described previously^{6,20,21}. Briefly, the Hsp27c NMR structure (PDB 2N3J) was surrounded with a 9-Å layer of cosolvent molecules (acetonitrile, isopropanol, or pyrimidine) and placed in a box of TIP3P water⁵⁰. The number of water molecules in each cosolvent simulation was adjusted such that a ratio of 5% cosolvent:water was achieved.

The force field parameters for the probes were obtained from our previous work⁵¹ and simulations were carried out in AMBER 12⁵² using the FF99SB force field⁵³. The SHAKE algorithm⁵⁴ was used to restrain bonds to hydrogen atoms, and a time step of 2 fs was used to integrate the equations of motion. Particle Mesh Ewald approximation as implemented for GPUs, PMEMCUDA⁵⁵ was used. Non-bonded interactions were limited to a 10-Å cutoff, and the Anderson Thermostat⁵⁶ was used to maintain temperature at 303 K (to match the temperature of the HSQC experiment). Hsp27c was subjected to an equilibration protocol to gradually increase the temperature and allow proper relaxation of all the atoms in the system. Using the NPT approach, ten simulations with 20 ns of sampling for each were

performed with Hsp27c and acetonitrile, isopropanol, and pyrimidine separately. A total of 600 ns of sampling was obtained.

The last five nanoseconds of the ten runs for each probe (the final 50 ns of sampling) were analyzed. The location of all atoms in the probe were binned onto a 0.5-Å grid, centered on the protein using the Ptraj⁵⁷ module of Amber Tools. The binned data was then converted to sigma values by subtracting the mean grid value from each grid point and dividing it by the standard deviation of all the grid points. This approach allowed us to visualize the propensity of a probe binding at a particular location akin to electron density. This normalization process allowed us to compare results across the three cosolvent simulations. The processed grids were then contoured at a value of 20σ to locate binding sites in our MixMD simulations. A high sigma value denotes heavily occupied sites.

4.2 Protein Purification.

This purification method was adapted from protocols kindly provided by the Klevit laboratory for expressing Hsp27c (residues 79–176 of full-length Hsp27). Terrific broth was inoculated with fresh overnight cultures of BL21 (DE3) cells containing the plasmids. Cultures were grown at 37°C with shaking at 150 rpm for 4–5 hours, to an OD₆₀₀ of ~1.0. After cooling to room temperature for about one hour, cultures were induced with 1 mL of 1 M IPTG (a final concentration of 1 mM). Lower concentrations of IPTG resulted in poor expression levels. Cultures were allowed to induce overnight at room temperature for about 18 hours, cells were harvested by centrifugation 4000 rpm for 10 min and pellets were stored at –80 °C until ready to purify. To lyse the cells, pellets were first suspended in 30 mL of lysis buffer per liter of cells using vortexing and pipetting. Lysis buffer contained 20 mM Tris, 100 mM NaCl, 10 mM EDTA, pH 8.0, and Roche Complete protease inhibitor (one mini tablet per 100 mL of buffer). The cells were lysed by two passes of microfluidization or 5 × 30 sec of sonication. The lysate was clarified by centrifugation at 15,000 rpm for 30 min, the supernatant was decanted, and PMSF was added to a final concentration of 300 μM. The protein was then subjected to a two-step ammonium sulfate precipitation as follows: Ammonium sulfate was slowly added to a final concentration of 16.9% (w/v). The salt was allowed to dissolve completely and the mixture was allowed to stir for an additional ten minutes at room temperature. The resulting mixture was centrifuged at 15,000 rpm for 30 minutes, the supernatant was decanted, and an additional 16.9% (w/v) ammonium sulfate was added to the supernatant. After stirring for ten minutes at room temperature, the resulting mixture was again centrifuged at 15,000 rpm for 30 minutes, resulting in precipitation of the sHsp protein in the pellet. Pellets were resuspended into MonoQ buffer A (20 mM Tris, pH 8.0) and dialyzed into 4 L of buffer A overnight. Protein was purified by MonoQ anion exchange chromatography with a gradient of 0 to 1 M NaCl over 20 column volumes. The wildtype proteins eluted at around 150 mM NaCl. Fractions containing protein were pooled and concentrated, then subjected to size exclusion chromatography using a SuperDex75 column in 50 mM NaPi, pH 7.5, 100 mM NaCl. Hsp27 core domain mutants were purified using the protocol for the wildtype protein, except that for mutations that changed the charge of the protein, the NaCl gradient used in the MonoQ purification step was altered accordingly. The R127W and S135F mutants are from the numbering sequence

in the full length Hsp27 proteins. In the Hsp27c, these mutation residues are R49W and S57F.

4.3 NMR studies.

HSQC spectra were acquired at 30 °C on a 600 MHz Bruker Avance II spectrometer equipped with cryoprobe, running Topspin version 2.1, or a Bruker DRX500 with a QCI Z-axis gradient cryoprobe, running Topspin version 1.3. Spectra were acquired on samples containing 150–200 µM Hsp27 core domain in 50 mM NaP_i, pH 7.5, 100 mM NaCl at 30 °C and always compared to solvent-controlled reference spectra. 256 scans were acquired per t1 values and spectral widths of 1500 Hz and 9615 Hz were used in the ¹H and ¹⁵N dimensions, respectively. Processing and spectral visualization was performed using rNMR⁵⁸ and Sparky⁵⁹. In the screen, the core Maybridge Ro3 collection (R3W010; Supplemental Table S1) of 1,000 fragments was used.

4.4 Differential Scanning Fluorimetry (DSF).

DSF experiments were performed using a ThermoFluor instrument (a generous gift from Johnson & Johnson) in Abgene black 384-well PCR plates. Each well received 7 µL of 10 µM Hsp27 in 50 mM NaPO₄, pH 7.4, 700 mM NaCl, 50 mM LiCl, and 100 µM 1,8-ANS, with test compounds added via pin tool (200 nL) to achieve final concentrations between 20 to 40 µM (1% DMSO). The chemical library was composed of the Spectrum MS2000 and NCC collections of known bioactives. Reactions were covered with silicon oil to limit evaporation. The plates were measured in up/down mode, which was empirically determined to give better signal-to-noise than the continuous ramp mode. Plates were heated from 65 °C to 80 °C in 1 °C increments, equilibrated for 130 seconds at each high temperature, cooled to 25 °C, and held for 10 sec at 25 °C prior to imaging with a single 10 second exposure for each temperature reading. Curves were fit using a sigmoid equation DSFWorld³⁵.

4.5. Synthetic procedures and analytical characterization.

¹H NMR spectra were obtained on Varian 300 MHz and 400 MHz spectrometers with CDCl₃ or d₆-DMSO as solvent, and chemical shifts are recorded in δ ppm. Mass spectrometry analysis was performed using a Micromass LCT with electrospray ionization.

4.6. Chemistry

4.6.1. General Chemistry Methods.—¹H NMR spectra were obtained on Varian 300 MHz and 400 MHz spectrometers with CDCl₃ or d₆-DMSO as solvent, and chemical shifts are recorded in δ ppm).

4.6.2. Synthesis of fragment screening hits 1–4.

4.6.2.1. 3-(thiophen-2-yl)aniline (1): Compound **1** was synthesized according to reported conditions⁶⁰. Briefly, 3-bromoaniline (0.172 g, 1.0 mmol, 1.0 eq) was dissolved in 10 mL THF to give a clear solution. Potassium carbonate (0.415 g, 3.0 mmol, 3.0 eq) dissolved in 2 mL H₂O was added, followed by 2-thienylboronic acid (0.166 g, 1.3 mmol, 1.3 eq). Tetrakis(triphenylphosphine)palladium(0) (0.034 g, 0.03 mmol, 0.03 eq) was then added, and the reaction solution was heated to reflux at 80°C for 12 hours until TLC in 50:50

hexanes:EtOAc indicated completion ($R_f = 0.5$); staining with ρ -anisaldehyde gave a purple spot for product. EtOAc (100 mL) was added to the reaction and it was extracted with H₂O (3 \times 35 mL), then brine (1 \times 35 mL), dried with Na₂SO₄, filtered, and evaporated under rotary vacuum to give a reddish brown oil. The crude product was purified by silica gel chromatography in 75:25 hexanes:EtOAc; pure fractions were combined and evaporated under reduced pressure to yield 1 as a bright yellow crystalline solid (144 mg, 83%): MS m/z 176.1 (M+H); ¹H NMR (400 MHz, d₆-DMSO): δ 7.67,7.61 (m, 5H), 7.28 (d, 1H), 7.17 (t, J = 4 Hz, 1H).

4.6.2.2. 2,3-dichlorobenzothioamide: 2,3-dichlorobenzothioamide was synthesized according to published conditions⁶¹. 2,3-dichlorobenzamide (192 mg, 1.0 mmol, 1 eq) was dissolved in 20 mL anhydrous THF and Lawesson's reagent (445 mg, 1.1 mmol, 1.1 eq) was added. The reaction was heated to reflux for 5 hours, then evaporated under rotary vacuum, washed with 3N HCl (10 mL), and neutralized with saturated NaHCO₃ (30 mL) before extracting with CH₂Cl₂ (3 \times 40 mL). The crude product was purified by silica gel chromatography in 80:20 hexanes: EtOAc to give 2,3-dichlorobenzothioamide as a yellow oil (183 mg, 88%; a repeat reaction gave 146 mg, 72%): MS m/z 206.0 (M+H); ¹H NMR (400 MHz, d₆-DMSO): δ 8.08 (bs, 1H), 7.46 (d, J = 7.6, 2H), 7.24,7.19 (m, 2H).

4.6.2.3. 2-(2,3-dichlorophenyl)thiazole-4-carboxylic acid (2): Compound 2 was synthesized according to reported conditions⁶². 2,3-dichlorobenzothioamide (210 mg, 1.02 mmol, 1 eq) was dissolved in 6 mL anhydrous THF, and bromopyruvic acid (170 mg, 1.02 mmol, 1 eq) was added. The solution was heated to reflux at 70°C for 14 hours, then cooled to room temperature and evaporated under reduced pressure. The resulting solid 2 was recrystallized from EtOAc (40 mL) to yield pale peach crystals (72 mg, 48%): ¹H NMR (400 MHz, d₆-DMSO): δ 13.22 (s, 1H), 8.70 (s, 1H), 8.11 (dd, J = 7.9, 1.4 Hz, 1H), 7.4 (dd, J = 8.0, 1.4 Hz, 1H), 7.58,7.56 (m, 1H).

4.6.2.4. (E)-3-(styrylthio)propanoic acid (3, E-olefin): 3-mercaptoproprionic acid (174 μ L, 2 mmol, 2 eq) was brought up in 12 mL THF and triethylamine (0.55 mL, 4 mmol, 4 eq) was added, followed by β -bromostyrene (128 μ L, 1 mmol, 1 eq). The mixture was heated to reflux while stirring for 1 h until TLC in 2.5% MeOH/CH₂Cl₂ + 0.05% AcOH indicated completion and the formation of a white precipitate was observed, which was thought to be the triethylamine HBr salt. This precipitate was filtered and rinsed with CH₂Cl₂ and the supernatant was stripped to give a clear oil. The crude material was purified by silica gel chromatography in 1.7% MeOH/CH₂Cl₂ to yield **3a** as 86% E-olefin (61.6 mg, 30%): ¹H NMR (400 MHz, CDCl₃): δ 11.2 (bs, 1H), 7.29,7.17 (m, 5H), 6.68 (d, J = 15.5 Hz, 1H), 6.52 (d, J = 15.5 Hz, 1H), 3.02 (t, J = 7.23, 2H), 1.66 (t, J = 7.80, 2H).

4.6.2.5. 2,3-dibromo-3-phenylpropanoic acid: Trans-cinnamic acid (1.0 g, 6.8 mmol, 1 eq) was dissolved in CHCl₃ (25 mL), and bromine (0.35 mL, 6.8 mmol, 1 eq) was added. The solution was heated to reflux for 30 minutes, with immediate formation of a precipitate upon heating, then cooled to 0 °C. The white precipitate was filtered and washed with cold CHCl₃ (25 mL) and dried to give pure 2,3-dibromo-3-phenylpropanoic acid 2.075g, 83%; a repeat reaction gave 1.88 g, 78%): MS m/z 308.2 (M+H). ¹H NMR (400 MHz, d₆-DMSO):

δ 13.7 (bs, 1H), 7.62 (d, J = 7.2 Hz, 2H), 7.37 (dd, J = 8, 1.6 Hz, 3H), 5.53 (d, J = 11.7 Hz, 1H), 5.31 (d, J = 11.7 Hz, 1H).

4.6.2.6. (Z)-(2-bromovinyl)benzene: 2,3-dibromo-3-phenylpropanoic acid (300 mg, 0.97 mmol, 1 eq) was dissolved in 10 mL of acetone dried over molecular sieves and Na_2SO_4 . Potassium carbonate (300 mg, 2.2 mmol, 2.2 eq) was added, and the resulting suspension was heated to reflux at 80 °C for one hour until TLC (5% MeOH/ CH_2Cl_2) indicated the absence of the starting material acid. The reaction mixture was evaporated under rotary vacuum to give an oily white solid, which was dissolved in CH_2Cl_2 (20 mL) and washed with aqueous 1N HCl (3 \times 30 mL). The combined aqueous layers were back-extracted with CH_2Cl_2 (3 \times 20 mL) and the combined organic layers were washed with brine (30 mL) and dried with Na_2SO_4 . Evaporation gave (Z)-(2-bromovinyl)benzene as a clear oil requiring no further purification (646 mg, 88%; a repeat reaction gave 470 mg, 64%): ^1H NMR (400 MHz, d_6 -DMSO): δ 7.71 (d, J = 7.6 Hz, 2H), (7.419, 7.344 (m, 3H), 7.087 (d, J = 7.8 Hz, 1H), 6.449 (d, J = 8.0 Hz, 1H).

4.6.2.7. (Z)-3-styrylthio)propanoic acid (3, Z-olefin): 3-mercaptopropionic acid (349 μL , 4 mmol, 2 eq) was brought up in toluene (10 mL) and triethylamine (0.87 mL, 6.3 mmol, 3 eq) and added slowly via addition funnel to a mixture of (Z)-(2-bromovinyl)benzene (0.384 g, 2.1 mmol, 1 eq) and tetrakis(triphenylphosphine)palladium(0) (0.116 g, 0.1 mmol, 0.05 eq) in toluene (10 mL). The mixture was heated to 90 °C under a reflux condenser while stirring for 12 h until TLC in 2.5% MeOH/ CH_2Cl_2 with AcOH indicated completion. The toluene was evaporated under rotary vacuum as an azeotrope with CH_2Cl_2 and the dried material was extracted from H_2O with CH_2Cl_2 (3 \times 30 mL), dried with brine (30 mL) and Na_2SO_4 . The crude product was a crude yellow oil which was purified by column chromatography on silica gel using a gradient of 0 to 2.5% MeOH in CH_2Cl_2 . The product ((Z)-3-styrylthio)propanoic acid was isolated as a white solid (161 mg, 37%; a repeat reaction on a larger scale gave 414 mg, 41%). ^1H NMR (400 MHz, d_6 -DMSO): δ 12.34 (bs, 1H), 7.62, 7.53 (m, 1H), 7.41, 7.18 (m, 3H), 6.48 (d, J = 11.0 Hz, 1H), 6.44 (d, J = 10.9 Hz, 1H), 3.00 (t, J = 6.99, 2H), 2.60 (t, J = 6.95, 2H).

4.6.2.8. 2-(2,4-difluorophenoxy)-3-nitropyridine: 2-(2,4-difluorophenoxy)-3-nitropyridine was synthesized according to published conditions⁶³. 2-chloropyridine (0.476 g, 3 mmol, 1 eq) and 2,4-difluorophenol (0.28 mL, 3 mmol, 1 eq) were combined in acetone (20 mL) with potassium carbonate (0.48 g, 3.45 mmol, 1.15 eq) and heated to reflux for 6 hours. The mixture was acidified with 1N HCl and extracted with ether (3 \times 30 mL). The combined organic layers were dried with brine (20 mL) and Na_2SO_4 , filtered, and the solvents were evaporated under reduced pressure to give a yellow oil. Addition of ~2 drops H_2O induced crystallization of the crude material, which was recrystallized from isopropanol to give 2-(2,4-difluorophenoxy)-3-nitropyridine as yellow crystalline solid (307 mg, 41%; a repeat reaction on a smaller scale gave 71 mg, 47%). MS m/z 253.1 (M+H); ^1H NMR (400 MHz, d_6 -DMSO): δ 8.60 (d, J = 9.6, 1H), 8.41 (d, J = 4.8, 1H), 7.51, 7.40 (m, 3H), 7.17 (t, J = 9.6, 1H).

4.6.2.9. 2-(2,4-difluorophenoxy)pyridin-3-amine (4): Compound **4** was synthesized according to published conditions⁶³. 2-(2,4-difluorophenoxy)-3-nitropyridine (150 mg, 0.60 mmol, 1 eq) was dissolved in 4 mL THF. A solution of sodium dithionite (Na₂S₂O₄, 1.5 g, 8.6 mmol, 14.5 eq) in 14.6 mL H₂O was added, and the mixture was allowed to stir at room temperature for 2.5 h at which point TLC in 80:20 hexanes:EtOAc indicated completion. The reaction mixture was quenched with saturated NaHCO₃ (10 mL) and extracted with CH₂Cl₂ (3 × 15 mL), dried with brine (30 mL) and Na₂SO₄. Evaporation of solvent under reduced pressure gave pure product **4** (as a white solid which was used without further purification (50 mg, 37%; a repeat reaction on a larger scale gave 156 mg, 30%): ¹H NMR (400 MHz, d₆-DMSO): δ 7.40, 7.29 (m, 2H), 7.12 (dd, J = 4.70, 1.17, 1H), 7.11, 6.82 (m, 2H), 8.20 (dd, J = 7.82, 4.70, 1H), 5.29 (s, 1H).

4.6.3. Synthesis of analogues of fragment screening hit **4**.

4.6.3.1. General procedure for electrophilic aromatic substitutions.: The substituted chlorobenzene 1.1 mmol, (1 eq) was dissolved in anhydrous DMF (2.5 mL) and the phenol component (1.1 mmol, 1 eq) was added. Cesium carbonate (1.3 mmol, 1.15 eq) was then added, and the reaction was allowed to proceed at room temperature until TLC indicated completion. Upon completion, the reaction mixture was filtered to remove the cesium carbonate, acidified with the addition of 1N HCl and extracted with CH₂Cl₂. The organic layers were washed with brine and dried with Na₂SO₄. Typically, the crude products were recrystallized from iPrOH or EtOAc, and the yield and characterization is reported for only the first crop of crystals. Where recrystallizations failed, products were purified by silica gel chromatography as indicated.

4.6.3.2 2-(2,4-difluorophenoxy)-5-nitropyridine (6): Compound **6** was synthesized according to an adapted protocol. To a solution of 2-chloro-5-nitropyridine (0.951 g, 6 mmol, 1 eq) in acetone (40 mL) was added 2,4-difluorophenol (0.56 mL, 6 mmol, 1 eq) and potassium carbonate (0.954 g, 6.9 mmol, 1.15 eq). The reaction mixture was heated to reflux overnight and then worked up according to the general protocol. The product was recrystallized from iPrOH to give pale yellow needles (1.10 g, 73%). ¹H NMR (400 MHz, d₆-DMSO): δ 9.02 (d, J = 2.8 Hz, 1H), 8.66 (dd, J = 9.0, 2.7 Hz, 1H), 7.54, 7.40 (m, 2H), 7.2 (t, J = 8 Hz, 1H).

4.6.3.3. 2-(4-fluorophenoxy)-5-nitropyridine (7): Compound **7** was recrystallized from iPrOH to give a yellow solid (96 mg, 46%): ¹H NMR (400 MHz, d₆-DMSO): δ 9.03 (d, J = 2.8 Hz, 1H), 8.62 (dd, J = 9.4, 2.8 Hz, 1H), 7.31, 7.27 (m, 5H).

4.6.3.4. 2,4-difluoro-1-(4-nitrophenoxy)benzene (8): Compound **8** was purified by silica gel column chromatography using 2% EtOAc in hexanes as eluent to give a clear oil (65 mg, 33%): ¹H NMR (400 MHz, d₆-DMSO): 8.24 (d, J = 8.8 Hz, 2H), 7.58, 7.46 (m, 2H), 7.25, 7.19 (m, 1H), 7.15 (d, J = 9.2 Hz, 2H).

4.6.3.5. 1-(4-fluorophenoxy)-2,4-dinitrobenzene (10): Compound **9** was recrystallized from iPrOH (107 mg, 50%): ¹H NMR (400 MHz, d₆-DMSO): δ 8.9 (s, 1H), 8.46, 8.42 (m, 1H), 7.41, 7.34 (m, 4H), 7.18, 7.15 (m, 1H).

4.6.3.6. 1-(2-fluorophenoxy)-2,4-dinitrobenzene (11): Compound **11** was recrystallized from iPrOH to give a yellow crystalline solid (165 mg, 53%): $^1\text{H NMR}$ (400 MHz, d_6 -DMSO): 8.90 (d, $J = 2.4$ Hz, 1H), 8.44 (dd, $J = 9.2, 2.4$ Hz, 1H), 7.54, 7.33 (m, 4H), 7.17 (d, $J = 9.2$ Hz, 1H).

4.6.3.7. 1-(2,4-difluorophenoxy)-2,4-dinitrobenzene (12): Compound **12** was recrystallized from iPrOH at 30°C overnight to give yellow needles (170 mg, 75%; a repeat reaction on a larger scale yielded 2.70 g, 62%): $^1\text{H NMR}$ (400 MHz, d_6 -DMSO): δ 8.9 (d, $J = 2.4$ Hz, 1H), 8.43 (dd, $J = 8, 2$ Hz, 2H), 7.68, 7.57 (m, 2H), 7.30, 7.22 (m, 2H).

4.6.3.8. 2-(2,4-difluorophenoxy)-1,3-dinitrobenzene (13): Compound **13** was recrystallized from iPrOH to give a yellow powder (94 mg, 42%): $^1\text{H NMR}$ (400 MHz, d_6 -DMSO): δ 7.69 (d, $J = 5.6$ Hz, 2H), 6.98 (t, $J = 5.6, 1\text{H}$), 6.69, 6.65 (m, 1H), 6.23, 6.18 (m, 2H).

4.6.3.9. phenoxy-3-nitro-pyridine (19): Compound **19** was synthesized according to an adapted protocol. To a solution of 2-chloro-5-nitropyridine (0.476 g, 3 mmol, 1 eq) in acetone (20 mL) was added phenol (0.28 mL, 3 mmol, 1 eq) and potassium carbonate (0.350 g, 3.45 mmol, 1.15 eq). The reaction mixture was heated to reflux overnight and then worked up according to the general protocol. The product was recrystallized from EtOAc (313 mg, 48%): $^1\text{H NMR}$ (400 MHz, d_6 -DMSO): δ 8.56 (dd, $J = 8, 1.6$ Hz, 1H), 8.39 (dd, $J = 4.8, 1.6$ Hz, 1H), 7.42 (t, $J = 7.6, 2\text{H}$), 7.36 (dd, $J = 8, 4.8$ Hz, 1H), 7.26 (t, $J = 7.6$ Hz, 1H), 7.20 (d, $J = 7.6$ Hz, 2H).

4.6.3.10. 6-(2,4-difluorophenoxy)pyridine-3-amine (20): Compound **20** was synthesized from 2-(2,4-difluorophenoxy)-5-nitropyridine using the same procedure used to prepare **4** and recrystallized from iPrOH to give 21 (90.6 mg, 23%): $^1\text{H NMR}$ (400 MHz, d_6 -DMSO): δ 7.41, 7.34 (m, 2H), 7.24 (dd, $J = 14.8, 9.2$ Hz, 1H), 7.10, 7.06 (m, 2H), 6.82 (d, $J = 8.8, 1\text{H}$), 5.04 (s, 2H).

4.6.3.11. 2-phenoxy-pyridin-3-amine (23): Compound **23** was synthesized from 3-nitro-phenoxy-pyridine using the same procedure used to prepare **4** and was used without further purification (24.7 mg, 22%): $^1\text{H NMR}$ (400 MHz, d_6 -DMSO): δ 7.37 (t, $J = 7.6$ Hz, 2H), 7.31 (dd, $J = 4.8, 1.2$ Hz, 1H), 7.14 (t, $J = 7.2$ Hz, 1H), 7.07 (m, 3H), 6.86 (dd, $J = 7.6, 4.8$ Hz, 1H), 5.23 (s, 2H).

4.6.3.12 2-(4-iodophenoxy)-3-nitropyridine (24): Compound **24** was synthesized according to an adapted protocol. To a solution of 2-chloro-5-nitropyridine (0.476 g, 3 mmol, 1 eq) in acetone (20 mL) was added 4-iodophenol (0.66 g, 3 mmol, 1 eq) and potassium carbonate (0.350 g, 3.45 mmol, 1.15 eq). The reaction mixture was heated to reflux overnight and then worked up according to the general protocol. The product was recrystallized from iPrOH (412 mg, 40%). $^1\text{H NMR}$ (400 MHz, d_6 -DMSO): δ 8.59 (d, $J = 8$ Hz, 1H), 8.42 (d, $J = 4.8$ Hz, 1H), 7.79 (d, $J = 8.8$ Hz, 2H), 7.4 (dd, $J = 8, 4.8$ Hz, 1H), 7.07 (d, $J = 8.4, 2\text{H}$).

4.6.3.13. 1-(3-fluorophenoxy)-2,4-dinitrobenzene (25): Compound **25** was recrystallized from iPrOH to give pale peach crystals (126 mg, 41%): (^1H NMR 400 MHz, d_6 -DMSO): δ 8.90 (d, $J = 2.8$ Hz, 1H), 8.47 (dd, $J = 9.2, 2.8$ Hz, 1H), 7.57 (dd, $J = 15.2, 8$ Hz, 1H), 7.31, 7.19 (m, 3H), 7.13 (d, $J = 7.6$ Hz, 1H).

4.6.3.14. 1-(2,4-dinitrophenoxy)-2,3,4-trifluorobenzene (26): Compound **26** was slowly recrystallized from iPrOH overnight at 30 °C to give pale yellow crystals (165 mg, 47%): ^1H NMR (400 MHz, d_6 -DMSO): δ 8.92 (d, $J = 2.8$ Hz, 1H), 8.44 (dd, $J = 9.2, 2.8$ Hz, 1H), 7.55, 7.39 (m, 3H).

4.6.3.15. 3-(2,4-dinitrophenoxy)-1,2,4,5-tetrafluorobenzene (27): Compound **27** was recrystallized from iPrOH to give cream colored crystals (88 mg, 43%): ^1H NMR (400 MHz, d_6 -DMSO): δ 8.95 (d, $J = 2.8$ Hz, 1H), 8.46 (dd, $J = 9.6, 2.8$ Hz, 1H), 8.11, 8.02 (m, 1H), 7.65 (d, $J = 9.6$ Hz, 1H).

4.6.3.16. 2,4-dichloro-1-(2,4-dinitrophenoxy)benzene (28): Compound **28** was recrystallized from iPrOH to give a pale yellow solid (230 mg, 100%): ^1H NMR (400 MHz, d_6 -DMSO): δ 8.93 (d, $J = 2.4$ Hz, 1H), 8.43 (dd, $J = 9.2, 2.4$ Hz, 1H), 7.94 (d, $J = 2$ Hz, 1H), 7.63, 7.53 (m, 2H), 7.18 (d, $J = 9.2$ Hz, 1H).

4.6.3.17. 2,4-dinitro 1-(4-(trifluoromethyl)phenoxy)-benzene (29): Compound **29** was recrystallized from iPrOH to give iridescent yellow crystals (132 mg, 52%): ^1H NMR (400 MHz, d_6 -DMSO): δ 8.11 (s, 1H), 7.67 (d, $J = 6$ Hz, 1H), 7.07 (d, $J = 5.2$ Hz, 2H), 6.64 (d, $J = 5.6$ Hz, 2H), 6.58 (d, $J = 6.4$, 1H).

4.6.3.18. 1-(2,4-dimethylphenoxy)-2,4-dinitrobenzene (30): Compound **30** was recrystallized from iPrOH to give fine yellow crystals (60 mg, 19%): ^1H NMR (400 MHz, d_6 -DMSO): δ 8.89 (d, $J = 2$ Hz, 1H), 8.41 (dd, $J = 9.2, 2$ Hz, 1H), 7.25 (s, 1H), 7.16 (d, $J = 8$ Hz, 1H), 7.09 (d, $J = 8.4$ Hz, 1H), 6.93 (d, $J = 9.6$ Hz, 1H).

4.6.3.19. 4-(2,4-dinitrophenoxy)benzaldehyde (31): Compound **31** was recrystallized from iPrOH to give a pale yellow solid (154 mg, 69%): ^1H NMR (400 MHz, d_6 -DMSO): δ 10.01 (s, 1H), 8.94 (d, $J = 2.8$, 1H), 8.52 (dd, $J = 9.6, 2.8$ Hz, 1H), 8.05 (dd, $J = 6.4, 2.0$ Hz, 2H), 7.43 (m, 3H).

4.6.3.20. 4-(2,4-dinitrophenoxy)benzoic acid (32): Compound **32** was purified by silica gel column chromatography using 50:50 hexanes:EtOAc, then recrystallized from iPrOH to give a yellow solid (62 mg, 21%): ^1H NMR (400 MHz, d_6 -DMSO): 13.08 (s, 1H), 8.95, 8.90 (m, 1H), 8.53, 8.46 (m, 1H), 8.26 (t, $J = 8.8$ Hz, 2H), 8.05 (m, 3H).

4.6.3.21. 2-(2,4-dinitrophenoxy)-naphthalene (34): Compound **34** was recrystallized from iPrOH to give yellow crystals (137 mg, 40%): ^1H NMR (400 MHz, d_6 -DMSO): δ 8.93 (d, $J = 2.4$ Hz, 1H), 8.43 (dd, $J = 8.8$ Hz, 2.4, 1H), 8.10 (d, $J = 8.8$ Hz, 1H), 8.0 (d, $J = 7.6$ Hz, 1H), 7.9 (d, $J = 7.6$ Hz, 1H), 7.81 (s, 1H), 7.61, 7.54 (m, 2H), 7.45 (dd, $J = 8.8, 2$ Hz, 1H), 7.25 (d, $J = 9.2$ Hz, 1H).

4.6.3.22. 1-(2,4-dinitrophenoxy)naphthalene (35): Compound **35** was synthesized on a smaller scale from 1-naphthol (38 mg, 0.26 mmol, 1 eq) and 1-chloro-2,4-dinitrobenzene (53 mg, 0.26 mmol, 1 eq) with cesium carbonate (98 mg, 0.3 mmol, 1.15 eq) and worked up as described in the general procedure. The product was recrystallized from iPrOH to give a yellow-orange solid (39 mg, 48%): $^1\text{H NMR}$ (400 MHz, d_6 -DMSO): δ 8.97 (d, $J = 2.4$ Hz, 1H), 8.37 (dd, $J = 9.2, 2.8$ Hz, 1H), 8.10 (d, $J = 8$ Hz, 1H), 7.98 (d, $J = 8$ Hz, 1H), 7.92 (d, $J = 8$ Hz, 1H), 7.65, 7.61 (m, 3H), 7.45 (d, $J = 7.2$ Hz, 1H), 7.01 (d, $J = 9.6$ Hz, 1H).

4.6.3.23. 5-(2,4-dinitrophenoxy)-1H-indole (36): Compound **36** was purified by column chromatography in 100% CH_2Cl_2 which gave incomplete separation. Only fractions that appeared to contain pure product (by TLC) were pooled, from which the product was isolated (42 mg, 18% purified yield): $^1\text{H NMR}$ (400 MHz, d_6 -DMSO): 9.12 (s, 1H), 8.94 (s, 1H), 8.66, 8.63 (m, 1H), 8.05 (dd, $J = 8.8, 1.6$ Hz, 1H), 7.45 (t, $J = 2.8$, 1H), 7.05 (d, $J = 8.4$, 1H), 6.98 (s, 1H), 6.7 (d, $J = 8.8$, 1H), 6.66 (s, 1H).

4.6.3.24. 2-(2,4-dinitrophenoxy)-6-methylpyridine (39): Compound **39** was recrystallized from iPrOH to give pale yellow needles (159 mg, 75%): $^1\text{H NMR}$ (400 MHz, d_6 -DMSO): δ 8.86 (d, $J = 2.8$ Hz, 1H), 8.70 (dd, $J = 9.2$ Hz, 2.4 Hz, 1H), 7.86 (t, $J = 7.6$ Hz, 1H), 7.70 (d, $J = 9.2$ Hz, 1H), 7.11 (d, $J = 7.6$ Hz, 1H), 7.07 (d, $J = 8.4$ Hz, 1H), 2.26 (s, 3H).

4.6.3.25. 1-(3,5-dimethylphenoxy)-2,4-difluorobenzene (40): Compound **40** was synthesized via a Chan-Lam coupling. To a stirring suspension of copper (II) acetate monohydrate (300 mg, 1.5 mmol, 1.5 eq) in CH_2Cl_2 (10 mL) containing molecular sieves was added 2,4-difluorophenol (95 μL , 1 mmol, 1 eq), pyridine (161 μL , 2 mmol, 2 eq), and 3,5-dimethylphenylboronic acid (330 mg, 2.2 mmol, 2.2 eq). The reaction was allowed to proceed at room temperature open to the air overnight (12 h), then filtered through Celite, acidified with 1N HCl (20 mL) and extracted with in CH_2Cl_2 (3×20 mL). The organic layers were washed with brine and dried with Na_2SO_4 , then evaporated under rotary vacuum to leave the crude product as a brown oil. The product was purified by silica gel chromatography using 5% EtOAc in hexanes as eluent to yield **40** as a pale yellow-orange oil (18 mg, 8%): $^1\text{H NMR}$ (400 MHz, d_6 -DMSO): δ 7.46, 7.43 (m, 1H), 7.25, 7.19 (m, 1H), 7.12, 7.07 (m, 1H), 6.73 (s, 1H), 6.55 (s, 2H), 2.22 (s, 6H).

4.6.3.26. 2-((2,4-dinitrophenyl)thio)pyridine (41): Compound **41** was synthesized according to the general procedure for electrophilic aromatic substitutions using 2-mercaptopyridine in place of a substituted phenol. The product was recrystallized from iPrOH to give yellow needles (184 mg, 86%): MS m/z 278.4 (M+H); $^1\text{H NMR}$ (400 MHz, d_6 -DMSO): δ 8.9 (d, $J = 3.65$, 1H), 8.68, 8.66 (m, 1H), 8.37 (dd, $J = 8.8, 2.5$ Hz, 1H), 7.98, 7.96 (m, 1H), 7.79 (d, $J = 7.82$ Hz, 1H), 7.53 (dd, $J = 7.6, 4.9$ Hz, 1H), 7.44 (d, $J = 9.0$, 1H).

4.6.3.27. 2,4-dinitro-N-phenylaniline (42): Compound **42** was recrystallized from iPrOH to give fuzzy, deep orange crystals (48 mg, 24%): $^1\text{H NMR}$ (400 MHz, d_6 -DMSO): δ 10.16 (s, 1H), 8.89 (d, $J = 2.4$ Hz, 1H), 8.22 (dd, $J = 9.60, 2.44$, 1H), 7.52 (t, $J = 7.6$ Hz, 2H), 7.40, 7.35 (m, 3H), 7.10 (d, $J = 9.6$ Hz, 1H).

4.6.3.28. (2,4-difluorophenyl)(2,4-dinitrophenyl)sulfane (43): Compound **43** was synthesized according to the general procedure but with 2,4-difluorothiophenol instead of a phenol. The reaction proceeded more quickly than the analogous reactions with phenols, requiring only 2 h at room temperature to proceed to completion by TLC (50:50 EtOAc:hexanes). The product was worked up according to the general procedure and the recrystallized with iPrOH to yield pure **43** (1.56, 76%): $^1\text{H NMR}$ (400 MHz, d_6 -DMSO): δ 8.89 (s, 1H), 8.31 (d, 1H), 7.91, 7.80 (m, 1H), 7.63, 7.59 (m, 1H), 7.37, 7.33 (m, 1H), 7.05 (d, $J = 9.2\text{H}$, 1H).

4.6.3.29. N-(2,4-difluorophenyl)-2,4-dinitroaniline (44): Compound **44** was synthesized according to the general procedure but with 2,4-difluoroaniline instead of a phenol and triethylamine as the base. The product was worked up according to the general protocol and used without further purification: **44** (1.56, 76%): $^1\text{H NMR}$ (400 MHz, d_6 -DMSO): δ 8.92 (d, 1H), 8.48, 8.43 (m, 2H), 7.68, 7.62 (m, 2H), 7.45 (d, 1H), 7.37 (d, 1H), 7.29 (d, 1H).

4.6.3.30. Methyl 4-(4-fluorophenoxy)benzoate (45): Compound **43** was synthesized via a Chan-Lam coupling. To a stirring suspension of 4-methoxycarbonylphenylboronic acid (32 mg, 0.18 mmol, 1 eq) in anhydrous CH_2Cl_2 (3.5 mL) containing **4**. To molecular sieves was added 4-fluorophenol (40 mg, 0.39 mmol, 2.2 eq), pyridine (31 μL , 0.36 mmol, 2 eq), and copper (II) acetate (48 mg, 0.267 mmol). The reaction was allowed to proceed at room temperature open to the air for 6 h, then was filtered through Celite, acidified with 1N HCl (20 mL) and extracted with in CH_2Cl_2 (3×20 mL). The organic layers were washed with brine and dried with Na_2SO_4 , then evaporated under rotary vacuum to leave the crude product as a brownish oil. The product was purified by silica gel chromatography using 5% EtOAc in hexanes as eluent to yield **45** as a colorless oil, which crystallized upon standing (68 mg, 82%): $^1\text{H NMR}$ (400 MHz, d_6 -DMSO): δ 7.94 (d, $J = 8.8$ Hz, 2H), 7.30, 7.26 (m, 2H), 7.19, 7.16 (m, 2H), 7.01 (d, $J = 8.8$ Hz, 2H).

4.6.3.31. 2,4-difluorophenyl 4-nitrobenzoate (46): 4-nitrobenzoyl chloride (2 g, 10.8 mmol, 1 eq) was dissolved in CH_2Cl_2 (40 mL). 2,4-difluorophenol (1.5 g, 11.9 mmol, 1.1 eq) was then added, followed by triethylamine (1.82 mL, 14.0 mmol, 1.3 eq). The reaction was allowed to stir at RT for 8 h, then worked up by addition of saturated aqueous NaHCO_3 (50 mL) and extracted with CH_2Cl_2 (3×30 mL). The combined organic layers were washed with brine and dried with Na_2SO_4 , then evaporated under rotary vacuum to leave the crude product as a yellow powdery solid, which was recrystallized from iPrOH to yield pure **44** (1.93 g, 64%; a repeat reaction on a larger scale yielded 4.91 g, 81%): $^1\text{H NMR}$ (400 MHz, d_6 -DMSO): δ 8.4 (d, $J = 10$ Hz, 4H), 7.61, 7.53 (m 2H), 7.23 (s, 1 H).

4.6.3.32. 2,4-dinitrophenyl 2,4-difluorobenzoate (47): 2,4-dinitrophenol stabilized with water (2.4 g, ~ 12.4 mmol, ~ 1.1 eq) was added to a 100 mL round-bottomed flask and dissolved in CH_2Cl_2 (40 mL). Activated powdered molecular sieves (4 \AA) were added to absorb the water from the reagent. 2,4-difluorobenzoyl chloride (1.4 mL, 11.3 mmol, 1 eq) was added via syringe, followed by triethylamine (1.82 mL, 14.0 mmol, 1.3 eq). The color of the solution immediately lightened from a vivid yellow to a pale yellow. The reaction was allowed to stir at RT for 8 h, then was worked up by addition of saturated aqueous NaHCO_3

(50 mL) and extracted with CH_2Cl_2 (3×30 mL). The combined organic layers were washed with brine and dried with Na_2SO_4 , then evaporated under rotary vacuum to leave the crude product as a bright yellow solid, which was recrystallized from iPrOH to yield pure **47** as yellow needles (2.44 g, 66%): ^1H NMR (400 MHz, d_6 -DMSO): δ 8.93 (d, $J = 2.4$ Hz, 1H), 8.71 (dd, $J = 9.2, 3.2$ Hz, 1H), 8.28, 8.22 (m, 1H), 8.00 (d, $J = 8.8$ Hz, 1H), 7.60, 7.55 (m, 1H), 7.40, 7.35 (m, 1H).

4.6.3.32. 4,4'-((4,6-dinitro-1,3-phenylene)bis(oxy))bis(1,3-difluorobenzene)

(48): Compound **48** was synthesized according to the general procedure for electrophilic aromatic substitutions, except that 2.5 eq of 2,4-difluorophenol (1.0 mL, 10.5 mmol) and 4 eq of cesium carbonate (5.5 g, 16.9 mmol) were reacted with 1,5-dichloro-2,4-dinitrobenzene (1.0 g, 4.2 mmol, 1 eq) in DMF (40 mL). TLC in 90:10 hexanes:EtOAc indicated that the reaction was complete after stirring for about 15 min at RT, at which point the reaction mixture was filtered to remove the cesium carbonate, acidified with the addition of 1N HCl (100 mL) and extracted with EtOAc (3×40 mL). The organic layers were washed with brine and dried with Na_2SO_4 . The crude product was recrystallized from isopropanol to yield **48** as pale yellow crystals (1.13 g, 63%): ^1H NMR (400 MHz, d_6 -DMSO): δ 8.98 (s, 1H), 7.55, 7.49 (m, 2H), 7.46, 7.40 (m, 2H), 7.17, 7.15 (m, 2H), 6.43 (s, 1H).

4.6.3.33. 1,4-bis(2,4-dinitrophenoxy)benzene (49): 1-chloro-2,4-dinitrobenzene (3.7 g, 18.2 mmol, 2 eq) was dissolved in DMF (50 mL) and hydroquinone (1 g, 9.1 mmol, 1 eq) was added. Triethylamine (0.78 mL, 20 mmol, 2.2 eq) was added, which caused a color change from bright yellow-orange through red, then brown, then green. After 3 h of stirring at RT TLC in 50:50 EtOAc:hexanes still showed starting material 1-chloro-2,4-dinitrobenzene, but also showed several other spots, so the reaction was stopped. The pH of the reaction mixture was determined to be 5.5, so it was neutralized with the addition of saturated aqueous NaHCO_3 (50 mL) and extracted with EtOAc (3×40 mL). The organic layers were washed with brine and dried with Na_2SO_4 . The crude product was recrystallized from isopropanol to yield **49** (720 mg, 18%): ^1H NMR (400 MHz, d_6 -DMSO): δ 8.92 (d, $J = 2.8$ Hz, 1H), 8.46 (dd, $J = 9.6, 2.8$ Hz, 2H), 7.45 (s, 4 H), 7.31 (dd, $J = 9.6, 2.8$ Hz, 2H).

Supplementary Material

Refer to Web version on PubMed Central for supplementary material.

Acknowledgements

The authors thank Rachel Klevit (University of Washington - Seattle) and Erik R. P. Zuiderweg (University of Michigan, Ann Arbor) for helpful advice. This work was supported by grants from the NIH (NS059690) to J.E.G., (GM065372) to H.A.C. and participation on the PSTP training grant (GM007767) to L.N.M.

References

1. Jakob U & Buchner J Assiting spontaneity: the role of Hsp90 and small Hsps as molecular chaperones. Trends in Biochemical Sciences 19, (1994).

2. Montfort RV, Slingsby C & Vierling E STRUCTURE AND FUNCTION OF THE SMALL HEAT SHOCK PROTEIN/ α -CRYSTALLIN FAMILY OF MOLECULAR CHAPERONES. in *Advances in Protein Chemistry* vol. 59 105 (2002).
3. Kappé G et al. The human genome encodes 10 α -crystallin-related small heat shock proteins: HspB1–10. *Cell Stress & Chaperones* 9 (2003).
4. Kriehuber T et al. Independent evolution of the core domain and its flanking sequences in small heat shock proteins. *FASEB j* 24, 3633–3642 (2010). [PubMed: 20501794]
5. Jehle S et al. Solid-state NMR and SAXS studies provide a structural basis for the activation of α B-crystallin oligomers. *Nat Struct Mol Biol* 17, 1037–1042 (2010). [PubMed: 20802487]
6. Rajagopal P, Liu Y, Shi L, Clouser AF & Klevit RE Structure of the α -crystallin domain from the redox-sensitive chaperone, HSPB1. *J Biomol NMR* 63, 223–228 (2015). [PubMed: 26243512]
7. Bagn  ris C et al. Crystal Structures of α -Crystallin Domain Dimers of α B-Crystallin and Hsp20. *Journal of Molecular Biology* 392, 1242–1252 (2009). [PubMed: 19646995]
8. Baranova EV et al. Three-Dimensional Structure of α -Crystallin Domain Dimers of Human Small Heat Shock Proteins HSPB1 and HSPB6. *Journal of Molecular Biology* 411, 110–122 (2011). [PubMed: 21641913]
9. Merck KB et al. Structural and Functional Similarities of Bovine α -Crystallin and Mouse Small Heat-shock Protein. *The Journal of Biological Chemistry* 268, 1046 (1993). [PubMed: 8093449]
10. Ito H et al. Hsp27 suppresses the formation of inclusion bodies induced by expression of R120 α B-crystallin, a cause of desmin-related myopathy. *CMLS, Cell. Mol. Life Sci* 60, 1217–1223 (2003). [PubMed: 12861387]
11. Christians ES, Ishiwata T & Benjamin IJ Small heat shock proteins in redox metabolism: Implications for cardiovascular diseases. *The International Journal of Biochemistry & Cell Biology* 44, 1632–1645 (2012). [PubMed: 22710345]
12. Almeida-Souza L et al. Increased Monomerization of Mutant HSPB1 Leads to Protein Hyperactivity in Charcot-Marie-Tooth Neuropathy. *J. Biol. Chem* 285, 12778–12786 (2010). [PubMed: 20178975]
13. Almeida-Souza L et al. Small Heat-Shock Protein HSPB1 Mutants Stabilize Microtubules in Charcot-Marie-Tooth Neuropathy. *Journal of Neuroscience* 31, 15320–15328 (2011). [PubMed: 22031878]
14. Alderson TR et al. Local unfolding of the HSP27 monomer regulates chaperone activity. *Nat Commun* 10, 1068 (2019). [PubMed: 30842409]
15. Alderson TR, Ying J, Bax A, Benesch JLP & Baldwin AJ Conditional Disorder in Small Heat-shock Proteins. *Journal of Molecular Biology* 432, 3033–3049 (2020). [PubMed: 32081587]
16. Marti-Renom MA et al. The AnnoLite and AnnoLyze programs for comparative annotation of protein structures. *BMC Bioinformatics* 8, S4 (2007).
17. Murray CW & Rees DC The rise of fragment-based drug discovery. *Nature Chem* 1, 187–192 (2009). [PubMed: 21378847]
18. Arrigo A-P et al. Hsp27 Consolidates Intracellular Redox Homeostasis by Upholding Glutathione in Its Reduced Form and by Decreasing Iron Intracellular Levels. *Antioxidants & Redox Signaling* 7, 11 (2005).
19. Ung PMU, Ghanakota P, Graham SE, Lexa KW & Carlson HA Identifying binding hot spots on protein surfaces by mixed-solvent molecular dynamics: HIV-1 protease as a test case: Identifying Binding Hot Spots on Protein Surfaces by MixMD. *Biopolymers* 105, 21–34 (2016). [PubMed: 26385317]
20. Ghanakota P, van Vlijmen H, Sherman W & Beuming T Large-Scale Validation of Mixed-Solvent Simulations to Assess Hotspots at Protein–Protein Interaction Interfaces. *J. Chem. Inf. Model* 58, 784–793 (2018). [PubMed: 29617116]
21. Ghanakota P & Carlson HA Moving Beyond Active-Site Detection: MixMD Applied to Allosteric Systems. *J. Phys. Chem. B* 120, 8685–8695 (2016). [PubMed: 27258368]
22. Lexa KW & Carlson HA Full Protein Flexibility Is Essential for Proper Hot-Spot Mapping. *J. Am. Chem. Soc* 133, 200–202 (2011). [PubMed: 21158470]
23. English AC, Groom CR & Hubbard RE Experimental and computational mapping of the binding surface of a crystalline protein. *Protein Engineering, Design and Selection* 14, 47–59 (2001).

24. Cimermancic P et al. CryptoSite: Expanding the Druggable Proteome by Characterization and Prediction of Cryptic Binding Sites. *Journal of Molecular Biology* 428, 709–719 (2016). [PubMed: 26854760]
25. Vajda S, Beglov D, Wakefield AE, Egbert M & Whitty A Cryptic binding sites on proteins: definition, detection, and druggability. *Current Opinion in Chemical Biology* 44, 1–8 (2018). [PubMed: 29800865]
26. Clark AR, Naylor CE, Bagn ris C, Keep NH & Slingsby C Crystal Structure of R120G Disease Mutant of Human α B-Crystallin Domain Dimer Shows Closure of a Groove. *Journal of Molecular Biology* 408, 118–134 (2011). [PubMed: 21329698]
27. Hochberg GKA et al. The structured core domain of B-crystallin can prevent amyloid fibrillation and associated toxicity. *Proceedings of the National Academy of Sciences* 111, E1562–E1570 (2014).
28. Delbecq SP, Jehle S & Kleivit R Binding determinants of the small heat shock protein, α B-crystallin: recognition of the ‘IxI’ motif: α B-crystallin: recognition of the ‘IxI’ motif. *The EMBO Journal* 31, 4587–4594 (2012). [PubMed: 23188086]
29. Rauch JN et al. BAG3 Is a Modular, Scaffolding Protein that physically Links Heat Shock Protein 70 (Hsp70) to the Small Heat Shock Proteins. *Journal of Molecular Biology* 429, 128–141 (2017). [PubMed: 27884606]
30. Hajduk PJ, Huth JR & Fesik SW Druggability Indices for Protein Targets Derived from NMR-Based Screening Data. *J. Med. Chem* 48, 2518–2525 (2005). [PubMed: 15801841]
31. Abad-Zapatero C Ligand efficiency indices for effective drug discovery. *Expert Opinion on Drug Discovery* 2, 469–488 (2007). [PubMed: 23484756]
32. Bembenek SD, Tounge BA & Reynolds CH Ligand efficiency and fragment-based drug discovery. *Drug Discovery Today* 14, 278–283 (2009). [PubMed: 19073276]
33. Makley LN et al. Pharmacological chaperone for α -crystallin partially restores transparency in cataract models. *Science* 350, 674–677 (2015). [PubMed: 26542570]
34. Shao H, Oltion K, Wu T & Gestwicki JE Differential scanning fluorimetry (DSF) screen to identify inhibitors of Hsp60 protein–protein interactions. *Org. Biomol. Chem* 18, 4157–4163 (2020). [PubMed: 32458889]
35. Wu T et al. Three Essential Resources to Improve Differential Scanning Fluorimetry (DSF) Experiments <http://biorxiv.org/lookup/doi/10.1101/2020.03.22.002543> (2020) doi:10.1101/2020.03.22.002543.
36. Dudich IV et al. Dimer structure as a minimum cooperative subunit of small heat-shock proteins. *Biochimica et Biophysica Acta (BBA) - Protein Structure and Molecular Enzymology* 1253, 163–168 (1995). [PubMed: 8519797]
37. Zavalov A et al. The effect of the intersubunit disulfide bond on the structural and functional properties of the small heat shock protein Hsp25. *International Journal of Biological Macromolecules* 22, 163–173 (1998). [PubMed: 9650071]
38. Verdine GL & Walensky LD The Challenge of Drugging Undruggable Targets in Cancer: Lessons Learned from Targeting BCL-2 Family Members. *Clinical Cancer Research* 13, 7264–7270 (2007). [PubMed: 18094406]
39. Zantema A, de Jong E, Lardenoije R & van der Eb AJ The expression of heat shock protein hsp27 and a complexed 22-kilodalton protein is inversely correlated with oncogenicity of adenovirus-transformed cells. *Journal of Virology* 63, 3368–3375 (1989). [PubMed: 2746733]
40. Strahler JR et al. Identification of two related markers for common acute lymphoblastic leukemia as heat shock proteins. *J. Clin. Invest* 85, 200–207 (1990). [PubMed: 2295696]
41. Michishita M et al. Phosphorylation of the Stress Protein Hsp27 is an Early Event in Murine Myelomonocytic Leukemic Cell Differentiation Induced by Leukemia Inhibitory Factor/D-Factor. *Biochemical and Biophysical Research Communications* 176, 979–984 (1991). [PubMed: 1903943]
42. Zhang Y et al. A Targetable Molecular Chaperone Hsp27 Confers Aggressiveness in Hepatocellular Carcinoma. *Theranostics* 6, 558–570 (2016). [PubMed: 26941848]
43. Sheng B et al. Increased HSP27 correlates with malignant biological behavior of non-small cell lung cancer and predicts patient’s survival. *Sci Rep* 7, 13807 (2017). [PubMed: 29062135]

44. Shi Y et al. Endothelium-targeted overexpression of heat shock protein 27 ameliorates blood–brain barrier disruption after ischemic brain injury. *Proc Natl Acad Sci USA* 114, E1243–E1252 (2017). [PubMed: 28137866]
45. Katsogiannou M et al. The Functional Landscape of Hsp27 Reveals New Cellular Processes such as DNA Repair and Alternative Splicing and Proposes Novel Anticancer Targets. *Mol Cell Proteomics* 3585 (2014).
46. Gibert B et al. Inhibition of heat shock protein 27 (HspB1) tumorigenic functions by peptide aptamers. *Oncogene* 30, 3672–3681 (2011). [PubMed: 21423207]
47. Gibert B, Simon S, Dimitrova V, Diaz-Latoud C & Arrigo A-P Peptide aptamers: tools to negatively or positively modulate HSPB1(27) function. *Phil. Trans. R. Soc. B* 368, 20120075 (2013). [PubMed: 23530261]
48. Heinrich J-C, Tuukkanen A, Schroeder M, Fahrig T & Fahrig R RP101 (brivudine) binds to heat shock protein HSP27 (HSPB1) and enhances survival in animals and pancreatic cancer patients. *J Cancer Res Clin Oncol* 137, 1349–1361 (2011). [PubMed: 21833720]
49. Heinrich JC et al. New HSP27 inhibitors efficiently suppress drug resistance development in cancer cells. *Oncotarget* 7, 68156–68169 (2016). [PubMed: 27626687]
50. Jorgensen WL, Chandrasekhar J, Madura JD, Impey RW & Klein ML Comparison of simple potential functions for simulating liquid water. *The Journal of Chemical Physics* 79, 926–935 (1983).
51. Lexa KW, Goh GB & Carlson HA Parameter Choice Matters: Validating Probe Parameters for Use in Mixed-Solvent Simulations. *J. Chem. Inf. Model* 54, 2190–2199 (2014). [PubMed: 25058662]
52. Case DA et al. Amber12 Reference Manual. (2012).
53. Hornak V et al. Comparison of multiple Amber force fields and development of improved protein backbone parameters. *Proteins* 65, 712–725 (2006). [PubMed: 16981200]
54. Ryckaert J-P, Ciccotti G & Berendsen HJC Numerical integration of the cartesian equations of motion of a system with constraints: molecular dynamics of n-alkanes. *Journal of Computational Physics* 23, 327–341 (1977).
55. Götz AW et al. Routine Microsecond Molecular Dynamics Simulations with AMBER on GPUs. 1. Generalized Born. *J. Chem. Theory Comput* 8, 1542–1555 (2012). [PubMed: 22582031]
56. Andersen HC Molecular dynamics simulations at constant pressure and/or temperature. *The Journal of Chemical Physics* 72, 2384–2393 (1980).
57. Roe DR & Cheatham TE PTRAJ and CPPTRAJ: Software for Processing and Analysis of Molecular Dynamics Trajectory Data. *J. Chem. Theory Comput* 9, 3084–3095 (2013). [PubMed: 26583988]
58. Lewis IA, Schommer SC & Markley JL rNMR: open source software for identifying and quantifying metabolites in NMR spectra: rNMR: metabolomics software. *Magn. Reson. Chem* 47, S123–S126 (2009). [PubMed: 19821464]
59. Lee W, Tonelli M & Markley JL NMRFAM-SPARKY: enhanced software for biomolecular NMR spectroscopy. *Bioinformatics* 31, 1325–1327 (2015). [PubMed: 25505092]
60. Vaisburg A, Moradei O & Leit S Inhibitors of Histone Deacetylase 172 (2005).
61. Colabufo NA et al. Multi-Drug-Resistance-Reverting Agents: 2-Aryloxazole and 2-Arylthiazole Derivatives as Potent BCRP or MRP1 Inhibitors. *ChemMedChem* 4, 188–195 (2009). [PubMed: 19140144]
62. Gillespie P, Goodnow JR RA, Kowalczyk A, Le K & Zhang Q Thiazoles as 11 Beta-HSD1 Inhibitors (2007).
63. Nakayama H, Ishihara K, Akiba S & Uenishi J Synthesis of N-[2-(2,4-Difluorophenoxy)trifluoromethyl-3-pyridyl]sulfonamides and Their Inhibitory Activities against Secretory Phospholipase A2. *Chem. Pharm. Bull* 59, 1069–1072 (2011).

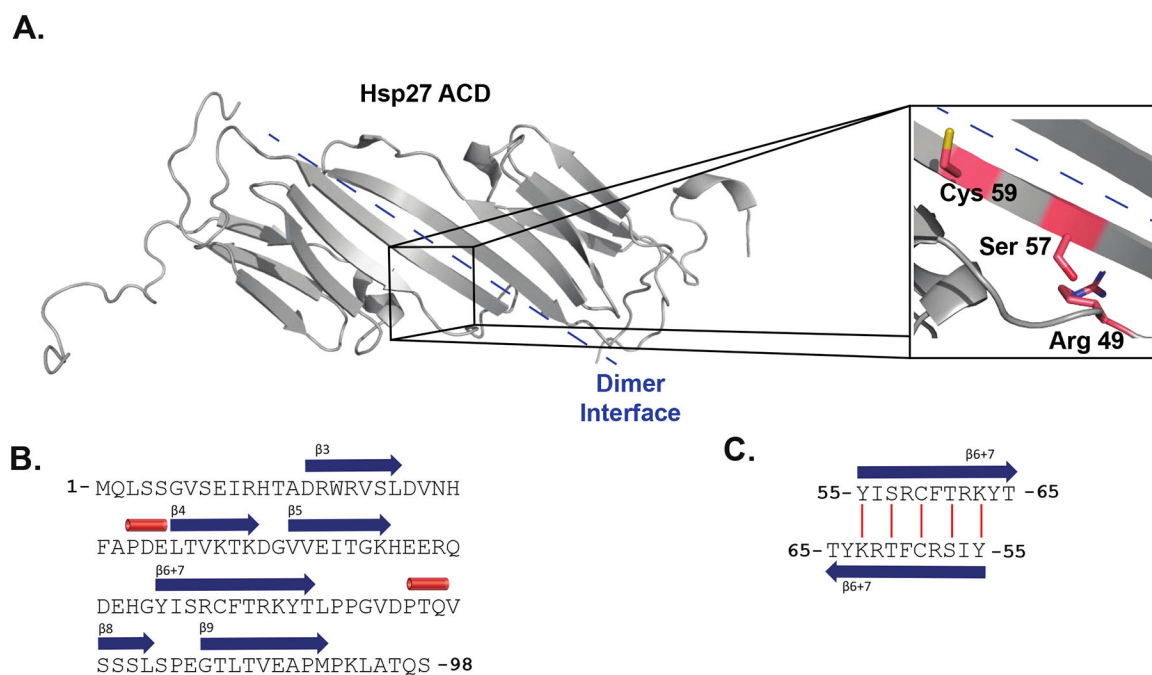


Figure 1. Disease-relevant perturbations occur at or near the Hsp27c homodimer interface.

A. cartoon representation of the Hsp27 core domain (Hsp27c) construct used in this work . Hsp27c residues 1–98 represent full-length Hsp27 residues 79–176 (PDB 2N3J) and Hsp27c residue numbering will be used throughout this work. Both Cys 59, which forms an intermolecular disulfide bond under certain conditions, and Ser 57, which is mutated in myopathy are at the dimer interface. Another myopathy-associated mutation occurs at Arg 49 which is in a flexible region. The amide backbone for Arg 49 is ~ 5 Å from the Hsp27 dimer interface despite the various sidechain orientations in this structure. **B.** Features of the primary sequence of the Hsp27c. **C.** A Π I register of dimer interface showing residue pairing. Red lines indicate cross-strand hydrogen bonding pairs in the A Π I register.

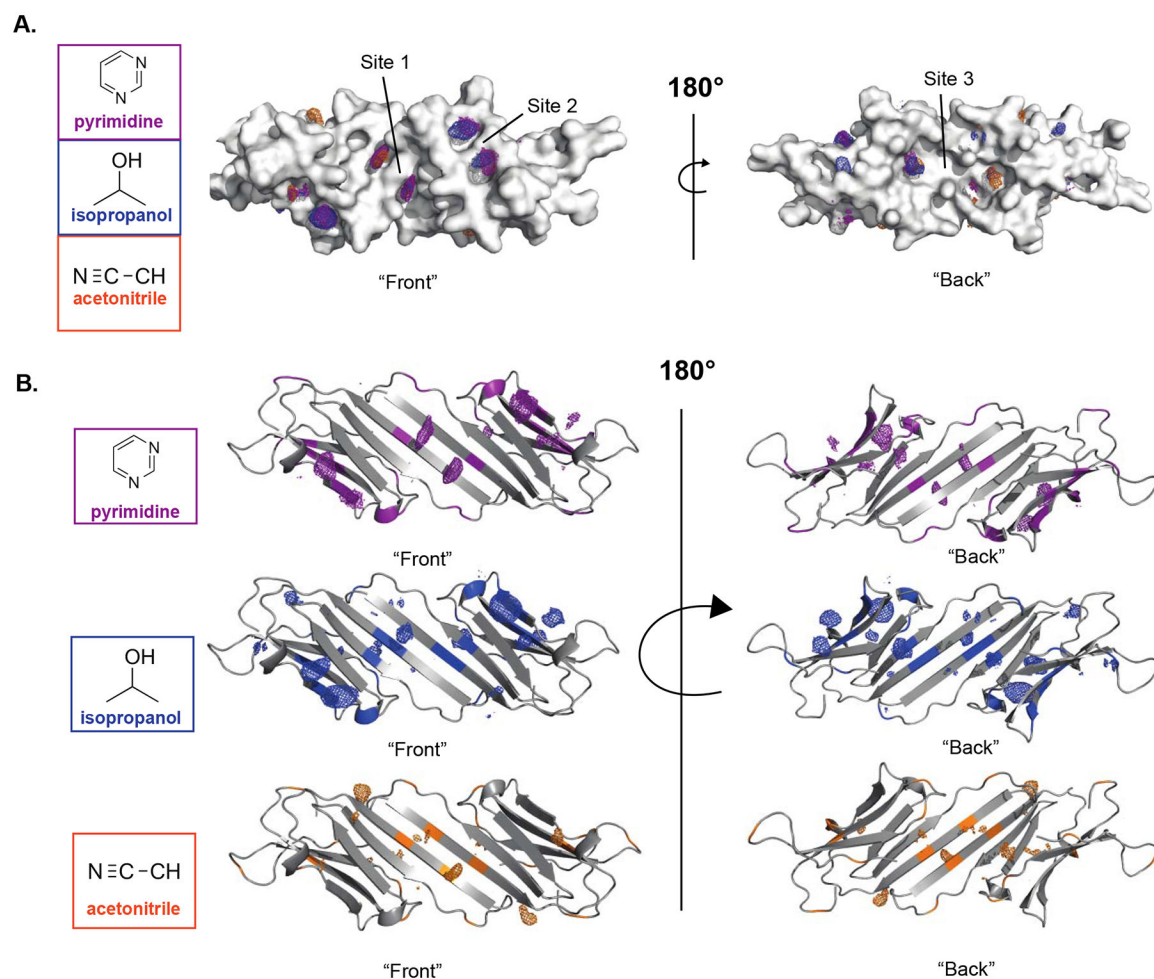


Figure 2. Identification of cryptic binding sites on Hsp27c.

A. Surface rendering of NMR structure of Hsp27 α B-crystallin domain, showing three regions where each solvent probe was highly localized. The sites are labeled as indicated in the order in which they were occupied (i.e. site 1 was most highly occupied by all three solvents and site 3 was the least occupied). **B.** Cartoon rendering of NMR structure of Hsp27 α B-crystallin domain, showing MixMD solvent probe occupancy maps and backbone chemical shift perturbations for solvent mapping NMR experiment. Backbone shifts were considered significant if they exceeded two standard deviations of the 5 mM data set for each solvent. Significant shift perturbations are shown for the 10 mM (0.08% v/v) pyrimidine, 20 mM (0.12% v/v) isopropanol, and 10 mM (0.04% v/v) acetonitrile concentrations.

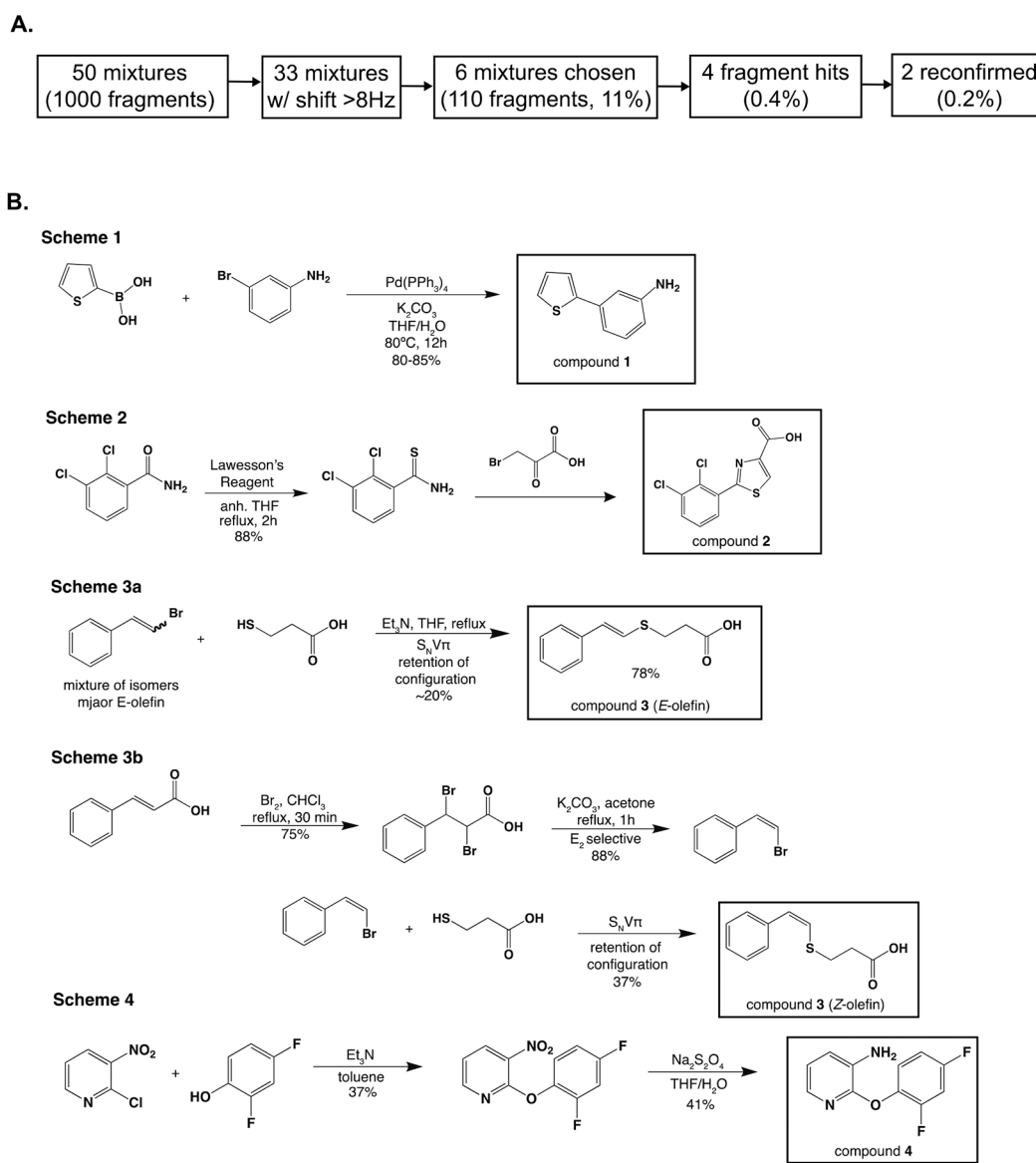


Figure 3. Identification of molecules that bind Site 3 by NMR fragment-based screens.

A. The screening workflow of the NMR-based fragment screen against Hsp27c **B.** Synthetic schemes used to resynthesize fresh powders of each of the four hit from the NMR fragment based screen.

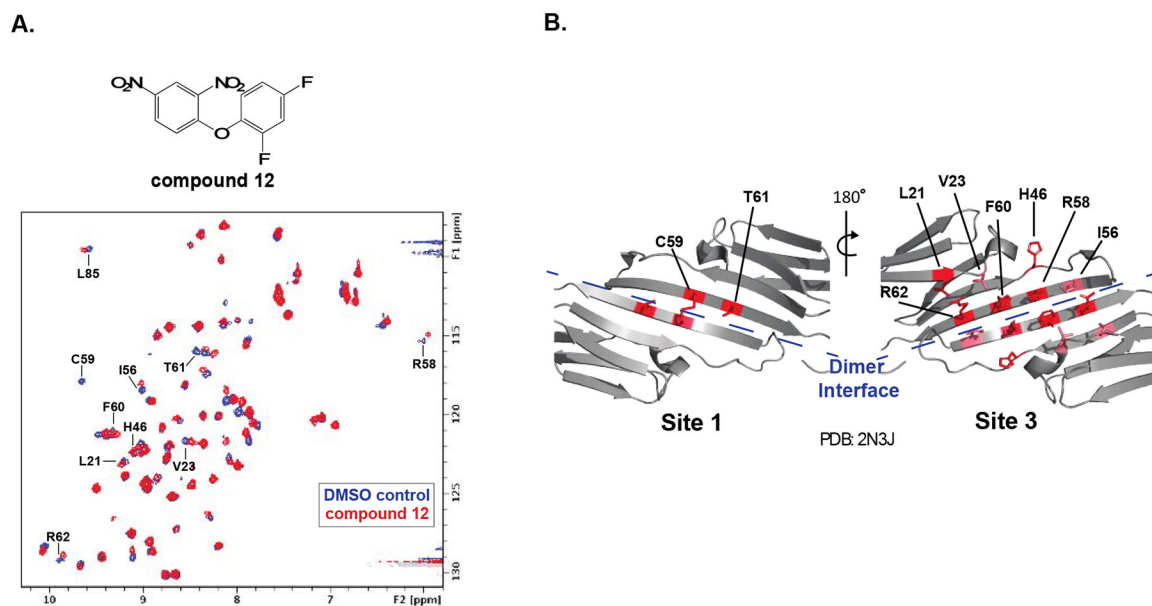
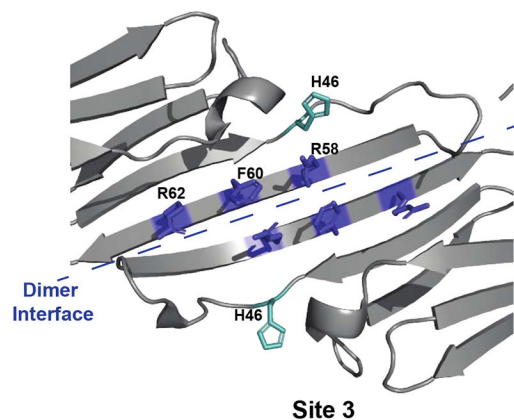


Figure 4. Compound 12 binds at the Hsp27 dimer interface.

A. Backbone chemical shift perturbations from **12** (1-(2,4-difluorophenoxy)-2,4-dinitrobenzene) binding to Hsp27c reveal that it binds at the Hsp27 dimer interface. The final concentrations of **12** and Hsp27 were 250 μ M (5% DMSO) and 125 μ M respectively (red). DMSO was added to the control condition to achieve a final DMSO concentration of 5% (blue). **B.** Residues that exhibit chemical shift perturbations upon **12** addition mapped onto Hsp27c (PDB: 2N3J). CSPs more than 2 standard deviations are colored red, and residues that are perturbed between 1 and 2 standard deviations are colored salmon.



Mutation	Residue Location	Apparent Affinity (μM)	Fold Change in Affinity vs Wild Type
C59A	Site 1	67 ± 12	4
T61L	Site 1	32 ± 5	2
L21A	Site 3	42 ± 4	3
V23A	Site 3	69 ± 12	4
I56A	Site 3	63 ± 10	4
H46A	Site 3	240 ± 20	15
R58A	Site 3	No Binding	N/A
F60A	Site 3	No Binding	N/A
R62A	Site 3	No Binding	N/A

Figure 5. Validation of compound binding site.

Backbone chemical shift perturbations from **12** (1-(2,4-difluorophenoxy)-2,4-dinitrobenzene) binding to Hsp27c do not permit differentiation between Site 1 and Site 3. **A.** Critical residues for **12** binding were identified by repeating HSQC NMR experiments with Hsp27 containing mutation of residues with significant chemical shift perturbations in the previous HSQC NMR experiment. The final concentrations of **12** and mutant Hsp27 were $250 \mu\text{M}$ (5% DMSO) and $125 \mu\text{M}$, respectively. Residues that contribute to **12** were mapped onto the Hsp27 structure (PDB 2N3J) with residues indispensable for binding shown in blue and residues with a large, but not obligate contribution to **12** binding shown in cyan.

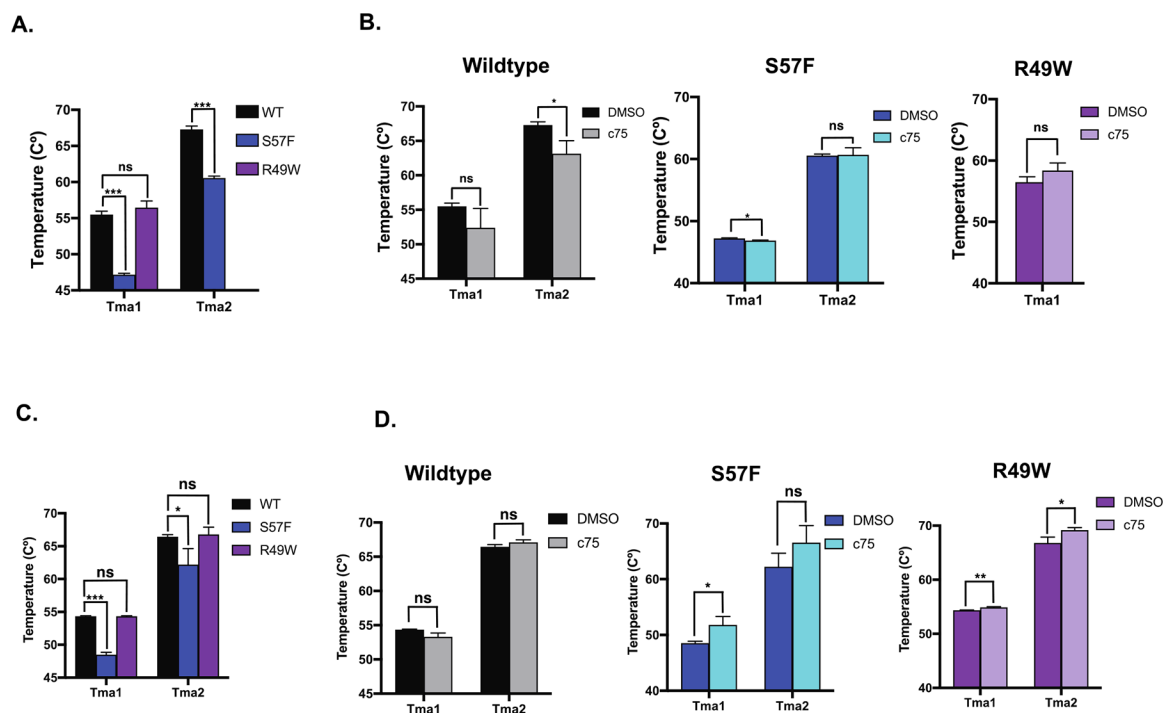


Figure 6. Differential Scanning Fluorimetry of disease associated mutants of Hsp27 with compound 12.

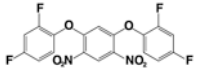
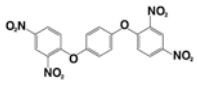
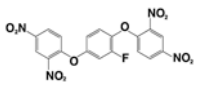
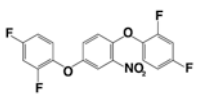
All DSF experiments were conducted in 384-well format. Each well received 7 μ L of 10 μ M Hsp27c in 50 mM NaPO₄, pH 7.4, 700 mM NaCl, 50 mM LiCl (A and B) with the addition of 5mM DTT (C and D). Environmentally sensitive dye 1,8-ANS was added for a final concentration of 100 μ M and **12** was added to achieve a final concentration of 10 μ M (1% DMSO). Control wells lacking **12** contained a final concentration of 1% DMSO. Plates were heated from 25°C to 95°C in 1 °C increments, equilibrated for 130 seconds at each high temperature, cooled to 25°C, and held for 10 sec at 25 °C prior to imaging with a single 10 second exposure for each temperature reading. All conditions were tested in triplicate and relationships were analyzed using an unpaired t-test in Prism GraphPad software (p-value: 0.120 (ns), 0.033 (*), 0.002 (**), <0.001 (***)). P-values were adjusted for multiple comparisons using the Holm-Sidak method. **A.** Comparison of thermal stability between the oxidized states of wildtype, S57F and R49W Hsp27. **B.** Comparison of oxidized Hsp27c thermal stability in the presence and absence of **12**. **C.** Comparison of thermal stability between the reduced states of wildtype, S57F and R49W Hsp27. **D.** Comparison of reduced Hsp27 thermal stability in the presence and absence of **12**.

Table 1.
Structure Activity Relationship for Compound 4 from NMR Fragment Screen.

An asterisk referred to compounds purchased from commercial sources.

Compound	Structure	HSQC Affinity	Ligand Efficiency (kcal/mol/non-H atom)
4		>1 mM	-
5		177 ± 16 μM	0.29
6		63 ± 3 μM	0.32
7		64 ± 7 μM	0.34
8		68 ± 9 μM	0.32
9		22 ± 5 μM	0.38
10		47 ± 10 μM	0.30
11		80 μM	x
12		16 ± 2 μM	0.32
13*		70 μM	x
24		No Binding	-

Compound	Structure	HSQC Affinity	Ligand Efficiency (kcal/mol/non-H atom)
25		No Binding	-
26		No Binding	-
27		No Binding	-
28		No Binding	-
29		No Binding	-
30		No Binding	-
31*		No Binding	-
32		No Binding	-
43		No Binding	-
44		No Binding	-
46		No Binding	-
47		No Binding	-

Compound	Structure	HSQC Affinity	Ligand Efficiency (kcal/mol/non-H atom)
48		No Binding	-
49		No Binding	-
50*		No Binding	-
51*		No Binding	-

Author Manuscript

Author Manuscript

Author Manuscript

Author Manuscript

Table 2.Affect of compound **12** on Hsp27 apparent melting temperature.

Oxidized Hsp27								
	T _{ma1} (°C)	T _{ma1} +12 (°C)	T _{ma1} (°C)	T _{ma1} p-value	T _{ma2} (°C)	T _{ma2} + 12 (°C)	T _{ma2} (°C)	T _{ma2} p-value
WT	55.5 ± 0.5	53.3 ± 1.6	-3.1	0.132	67.3 ± 0.5	63.1 ± 1.9	-4.2	0.021
S57F	47.2 ± 0.1	46.8 ± 0.1	-0.4	0.014	60.5 ± 0.3	60.7 ± 1.2	0.1	0.857
R49W	56.4 ± 0.9	58.3 ± 1.3	1.9	0.107	ND	ND	ND	ND
Reduced Hsp27								
	T _{ma1} (°C)	T _{ma1} +12 (°C)	T _{ma1} (°C)	T _{ma1} p-value	T _{ma2} (°C)	T _{ma2} + 12 (°C)	T _{ma2} (°C)	T _{ma2} p-value
WT	54.3 ± 0.1	53.5 ± 0.6	-1.0	0.040	66.4 ± 0.4	67.1 ± 0.4	0.7	0.100
S57F	48.5 ± 0.5	51.8 ± 1.5	3.3	0.023	62.2 ± 2.5	66.5 ± 1.2	4.3	0.133
R49W	54.3 ± 0.1	54.9 ± 0.2	0.6	0.006	66.8 ± 1.1	69.1 ± 0.5	2.4	0.029